Damage progression and strength prediction of open-hole CFRP laminates containing ply gaps

Onodera, Sota
Department of Aeronautics and Astronautics, Kyushu University

Kawahara, Koki
Department of Aeronautics and Astronautics, Kyushu University

Yashiro, Shigeki
Department of Aeronautics and Astronautics, Kyushu University

https://hdl.handle.net/2324/7152026

出版情報：Engineering Fracture Mechanics. 293, pp.109681-, 2023-12-01. Elsevier
バージョン：
権利関係：

Damage progression and strength prediction of open-hole CFRP laminates containing ply gaps

Sota Onodera[a,*], Koki Kawahara[a], Shigeki Yashiro[a]

[a]Department of Aeronautics and Astronautics, Kyushu University, 744 Motooka, Nishi-ku, Fukuoka 819-0395, Japan

[*]Corresponding Author: sota.onodera@aero.kyushu-u.ac.jp (Sota Onodera)

Abstract

Although automated fiber placement manufacturing can improve productivity, gaps and overlaps of plies occur due to the low position accuracy of the robot arm. This study develops the ply-by-ply shell layer model to investigate the mechanical effects of a gap on the damage progression and strength of composite laminates with a hole. The gaps and a hole are modeled independently of the mesh using the extended finite element method (XFEM) to reduce the preprocessing and computational costs using a simple square mesh. The opening of the resin rich area of the gap is represented by applying the cohesive zone model to the crack surface. The open hole tensile analysis was performed on a laminate with gaps. The predicted strength of specimen with gaps agrees well with the experiment and is slightly higher than that of specimen without gaps because the gap opening reduces the stress concentration at the hole.

Keywords: Polymer matrix composites, Cohesive zone modelling, Damage mechanics, Finite element analysis

1. Introduction

The productivity of carbon fiber reinforced plastic (CFRP) structures must be increased to meet the growing demand for composite structures in the aerospace fields. Since 1970s, the automated technologies of the layup process of CFRP laminates have been continuously developed to improve productivity and reduce fabrication costs [1,2]. Automated fiber placement (AFP) is one of the automated technologies used for automatic fabrication of the CFRP components of aircrafts. It utilizes a robot arm head with narrow width CFRP prepreg slices. The AFP robot arm head path is variable, which allows the variable curvature and angle paths to be used for manufacturing the multi-stiffened CFRP laminates [3].

Although AFP manufacturing technology improves productivity of composite laminates, it can introduce several types of manufacturing defects. Denkena et al. [4] conducted the analysis of AFP production process.

They mentioned that processing time of placing slit tapes to manufacture the fuselage panel is only 46% while remaining time is spent in manually inspecting every ply, correcting defects, and other activities/processes. A detailed classification of manufacturing defect types in AFP manufacturing is provided by Harik et al. [4] and Heinecke et al. [5]. Among these defects, gaps and overlaps of plies are difficult to avoid due to the low position accuracy of the robot arm.

Fig. 1 shows a gap and overlap parallel to the fiber direction in a composite laminate. Because a resin rich region is generated at the gap [6], the structural strength can be influenced by the gap. In addition, fibers in neighboring plies are curved in the through-thickness direction along the gap/overlap. The local structural change can lead to degraded mechanical properties. However, the impact of gap/overlap on the mechanical properties is unclear. Generally, these defects occur simultaneously, and the fact that their effects vary depending on loading conditions and structural shapes makes them perplexing. The design-allowable strength of composite laminates must be low for their application in aircraft structures. Therefore, it is necessary to understand the essential nature of damage and fracture phenomena caused by the presence of defects.

Several experimental studies have clarified the influence of gap/overlap on composite laminate strength [7–17]. Croft et al. [12] investigated the ultimate strengths of composite laminate with gaps/overlaps subjected to tensile, compressive, or shear loads. As a result, the fiber waviness of 0° ply mainly decreases the open-hole compressive and in-plane shear strength. Lan et al. [14,16] demonstrated that the compressive strength of composite laminate with gap and overlap defects is improved by reducing the fiber waviness using the cowl plate. Marouene et al. [17] found that the open-hole compressive strength depends on the defect position against the hole in the laminate. The open-hole compressive strength is considerably reduced when the gap parallel to compressive loading is located at the center of the hole. Nguyen et al. [9,10] conducted a comprehensive experimental study of the influence of gaps/overlaps on the tensile/compressive strength and damage progression. They concluded that the tensile/compressive strength decreases as the gap width increases and that the effect of overlap on tensile/compressive strength is relatively small. The experimental studies indicate that the type and distribution of defects will have a significant effect on the strength properties of CFRP laminates.

Many of the experimental studies mentioned above analyzed composite laminates with defects controlled using hand lamination and experimentally measured their stiffness and strength. However, clear trends of the impact of defects on mechanical properties still remain unclear. An experimental approach alone is not efficient because the type, distribution, and shape of defects vary considerably. Thus, numerical studies [17–21] have also been conducted. Li et al. [19] developed 3D meshing tools of ply-by-ply finite element models with gaps and overlaps. In their study, the ply waviness is explicitly modeled by varying the solid element thickness, and the matrix crack and delamination are modeled using the cohesive zone model (CZM). Moreover, the fiber failure is predicted by applying the Weibull statistical failure criterion. They investigated the influence of gaps and overlaps on composite laminate tensile/compressive strength using their developed model. Nguyen et al. [21] generated the 3D solid finite element meshes of microstructures with gaps and overlaps using optical micrographs of specimen free edge. Using rigorously modeled meshes, the finite element analysis (FEA) of the laminate with gaps/overlaps perpendicular to the loading direction was performed, and their obtained numerical results qualitatively reproduced the strength and in-plane damage progression of experimental observations. Although these meshing tools can explicitly model the geometry of gaps and overlaps, it tremendously increases the computational cost due to complex finite element meshes. The finite element mesh generation tends to be a complex and laborious task in the analysis of composite laminates with inherent gaps and overlaps due to microstructural variation near the defects. Therefore, the development of an FEA tool that can easily model microstructures with gaps and overlaps is indispensable for the numerical simulation of the effects of gaps and overlaps at low computational costs and for the design and development of composite structures.

This study develops the ply-by-ply shell layer model to investigate the mechanical effects of a gap on the damage progression and strength of composite laminates with a hole. In particular, a hole and gaps are modeled independently of the finite element meshes using the extended finite element model (XFEM) to simplify the mesh and reduce the computational costs. Considering that the gap area is filled with resin after curing, bonding and opening of the gap area are represented by applying the cohesive zone model (CZM) to the crack surface of the XFEM. To verify the proposed model, the open hole tensile (OHT) analysis of a quasi-isotropic CFRP laminate without gaps was conducted and its results compared with the experimental results reported by Hallett et al. [22] and Song et. al. [23]. After the verification, the proposed model results are compared with experimental results on ultimate tensile strength and damage progression at final failure in open hole quasi-isotropic CFRP laminates with manually introduced gaps. These test specimens with gaps were subjected to cowl plates during resin curing to minimize fiber waviness.

Therefore, the effect of undulation was negligible, and the resin-filled gap is simplified as a crack by the XFEM to investigate the effect of the gap on the ultimate tensile strength.

The remainder of this paper is structured as follows. Section 2 describes the proposed ply-by-ply shell layer model, which is a numerical analysis model that simplifies the finite element mesh, thus reducing the computational costs. Section 3 describes the verification analysis of an open hole quasi-isotropic CFRP laminate without gaps. In Section 4, the OHT analysis of quasi-isotropic CFRP laminates with or without gaps using the proposed model is discussed, and the effect of gaps on strength is investigated. In Section 5, the conclusion of this study is presented.

2. Numerical Model

2.1 Ply-by-Ply shell layer model

The ply-by-ply shell layer model based on incremental static implicit FEA was developed to simulate the damage progression and strength of open hole CFRP laminates with gaps for simplified modeling and low computational costs. The CFRP ply was assumed as a linear transversely isotropic body with infinitesimal-deformation. The Newton-Raphson method was used to calculate the displacement increment for each incremental step by solving the equilibrium equation between the internal and external forces. The in-house FEA code was developed in Fortran language.

Fig. 2 shows the schematic figure of ply-by-ply shell layer model. The laminated structure was modeled with shell elements for each ply, and each shell layer (ply) was connected to a CZM that represented delamination. The matrix cracking and the fiber breakage were considered using continuum damage mechanics (CDM). The XFEM was used to model a hole and gaps independently of the finite element mesh. This implies that the gaps were modeled as built-in cracks. Closing and opening of the filled-in gap were predicted by applying the CZM to the crack surface of the XFEM. The gaps expressed by cracks on shell elements with a simple square mesh were modeled independently of the mesh to reduce computational cost. The same mesh is applicable for the hole and gaps of various geometries, which saves pre-processing and improves the consistency of the analysis. Each of these models is detailed below. The ply-by-ply shell layer model assumes that the same mesh shells is used for each layer. Therefore, it is not possible to uncouple the shell layer and CZM using kinematic constraints.

2.2 MITC shell element

The shell elements can be used to model the thin CFRP ply. To avoid shear locking owing to the low plate thickness, a four-node mixed interpolation of the tensorial component (MITC) shell element [24,25] was employed, as shown in Fig. 3.

Using the natural coordinate system (isoparametric coordinate system of the shell element) (r_1, r_2, r_3), the displacement $\boldsymbol{u}$ within a shell element in the global coordinate system (x, y, z) is given as follows.

$$\boldsymbol{u}(r_1, r_2, r_3) = \sum_{I=1}^{4} \boldsymbol{N}_{\mathrm{std}}^{I} \boldsymbol{U}_{\mathrm{std}}^{I} = \sum_{I=1}^{4} N^I(r_1, r_2) \left[\boldsymbol{I}_3 \quad \frac{t}{2} r_3 [-\boldsymbol{V}_2^I \quad \boldsymbol{V}_1^I] \right] \boldsymbol{U}_{\mathrm{std}}^{I}, \tag{1}$$

where, I denotes the node number, $\boldsymbol{U}_{\mathrm{std}}^{I} = \left[u_x^I \quad u_y^I \quad u_z^I \quad \alpha^I \quad \beta^I \right]^{\mathrm{T}}$ is the generalized nodal displacement vector composed of translational displacement (u_x^I, u_y^I, u_z^I) and rotation (α^I, β^I), $\boldsymbol{N}_{\mathrm{std}}^{I}$ is the generalized shape function corresponding to $\boldsymbol{U}_{\mathrm{std}}^{I}$, $N^I(r_1, r_2)$ is the shape function of 4-node isoparametric element, $\boldsymbol{I}_3$ is the identity matrix of size three, t is thickness, and $\boldsymbol{V}_1^I$, $\boldsymbol{V}_2^I$, and $\boldsymbol{V}_3^I$ are unit basis vectors in natural coordinate system, where $\boldsymbol{V}_3^I$ is director vector. The motion of a shell element is described by three nodal displacements (u_x^I, u_y^I, u_z^I) and two rotations (α^I, β^I) in the neutral plane. Therefore, the total number of nodes and degrees of freedom was smaller than that of 3D solid elements, which reduced the modeling effort and computational cost. Two integration points were set in each direction (8 points in total).

In the MITC shell element, the out-of-plane shear strain components, γ_{13} and γ_{23}, are reinterpolated by the out-of-plane shear strain at four sampling points A, B, C, and D as follows.

$$\gamma_{13} = \frac{1}{2}(1 + r_2)\gamma_{13}^{A} + \frac{1}{2}(1 - r_2)\gamma_{13}^{C} \tag{2}$$

$$\gamma_{23} = \frac{1}{2}(1 + r_1)\gamma_{23}^{D} + \frac{1}{2}(1 - r_1)\gamma_{23}^{B} \tag{3}$$

The superscripts A, B, C, and D denote each sampling point in Fig. 3. Shear locking can be avoided using Eqs. (2) and (3).

Compared to first-order isoparametric solid elements and MITC shell elements, MITC shell elements have a smaller total degree of freedom (DoF) per element. The first-order isoparametric solid element consists of 8 nodes with 3 degrees of freedom per node. In contrast, the MITC shell element has 4 nodes and 5 degrees of freedom per node. The total number of DoF of the isoparametric solid element was 24, and that of the MITC shell element was 20. Therefore, the total number of DoF per element is smaller for the MITC shell element, and the smaller dimensions of the element stiffness equations lead to lower computational cost. Furthermore, first-order isoparametric solid elements require 2 or 3 layers of mesh per ply owing to shear locking. However, the MITC shell elements can be represented by only one shell layer per layer because shear locking can be avoided. The ability of the MITC shell elements to avoid shear locking is discussed in Appendix A. The ability of the MITC shell elements to correctly perform delamination propagation analysis when the CZM was applied between the MITC shell layers is discussed in Appendix B.

2.3 CZM

The CZM represents delamination or crack opening by decreasing the traction in response to increase of relative displacement between elements. The CZM proposed by Camanho et al. [26] was used to predict mixed-mode crack opening. The cohesive element connected each shell layer consists of 8 nodes (green points), as shown in Fig. 4, and the traction between the elements was applied in the direction of decreasing relative displacement. The zero-thickness cohesive element was placed between the top surface of the lower shell element and the bottom surface of the upper shell element. The unit basis vectors in the directions of the modes I, II, and III crack openings are denoted as $\tilde{\boldsymbol{e}}_{\mathrm{I}}$, $\tilde{\boldsymbol{e}}_{\mathrm{II}}$, and $\tilde{\boldsymbol{e}}_{\mathrm{III}}$, respectively. The local coordinate system ($\tilde{X}_{\mathrm{I}}$, $\tilde{X}_{\mathrm{II}}$, $\tilde{X}_{\mathrm{III}}$) is defined to represent the constitutive laws of the CZM. $\tilde{X}_i$ (i = I, II, III) is the coordinate component along the direction of mode i, which corresponds to the unit basis vector $\tilde{\boldsymbol{e}}_i$.

The relation between the traction $\tilde{\boldsymbol{T}} = [\tilde{t}_{\mathrm{I}} \quad \tilde{t}_{\mathrm{II}} \quad \tilde{t}_{\mathrm{III}}]^{\mathrm{T}}$ and the relative displacement $\tilde{\boldsymbol{\Delta}} = [\tilde{\delta}_{\mathrm{I}} \quad \tilde{\delta}_{\mathrm{II}} \quad \tilde{\delta}_{\mathrm{III}}]^{\mathrm{T}}$ in the local coordinate system ($\tilde{X}_{\mathrm{I}}$, $\tilde{X}_{\mathrm{II}}$, $\tilde{X}_{\mathrm{III}}$) is given by the following expression.

$$\tilde{\boldsymbol{T}} = \tilde{\boldsymbol{D}}\tilde{\boldsymbol{\Delta}} = \begin{bmatrix} (1-d)K\dfrac{\langle\tilde{\delta}_{\mathrm{I}}\rangle}{\tilde{\delta}_{\mathrm{I}}} + K\left(1-\dfrac{\langle\tilde{\delta}_{\mathrm{I}}\rangle}{\tilde{\delta}_{\mathrm{I}}}\right) & 0 & 0 \\ 0 & (1-d)K & 0 \\ 0 & 0 & (1-d)K \end{bmatrix} \begin{bmatrix} \tilde{\delta}_{\mathrm{I}} \\ \tilde{\delta}_{\mathrm{II}} \\ \tilde{\delta}_{\mathrm{III}} \end{bmatrix}, \tag{4}$$

where, K is penalty stiffness, d is damage variable, $\langle \quad \rangle$ indicates Macaulay brackets defined as $\langle x\rangle = \max(0, x)$, subscripts I, II, and III denote modes I, II, and III, respectively. The relative displacement $\tilde{\boldsymbol{\Delta}}$ between the shell element surfaces can be expressed as follows.

$$\tilde{\boldsymbol{\Delta}} = \boldsymbol{R}\{\boldsymbol{u}_{Upper}(r_1, r_2, -1) - \boldsymbol{u}_{Lower}(r_1, r_2, +1)\}, \tag{5}$$

where, the subscripts *Upper* and *Lower* denote the upper and lower shell elements, respectively, and $\boldsymbol{R}$ is the coordinate transformation matrix used to transform $\boldsymbol{u}$ defined in the global coordinate system in Eq. (1) into that in the local coordinate system ($\tilde{X}_{\mathrm{I}}$, $\tilde{X}_{\mathrm{II}}$, $\tilde{X}_{\mathrm{III}}$).

The CZM considering mixed modes [26] was employed as the damage model. The relative displacement $\tilde{\delta}$ under mixed modes is expressed as follows.

$$\tilde{\delta} = \sqrt{\langle\tilde{\delta}_{\mathrm{I}}\rangle^2 + \left(\tilde{\delta}_{\mathrm{II}}\right)^2 + \left(\tilde{\delta}_{\mathrm{III}}\right)^2} = \sqrt{\langle\tilde{\delta}_{\mathrm{I}}\rangle^2 + \left(\tilde{\delta}_{\mathrm{shear}}\right)^2}, \tag{6}$$

where, $\tilde{\delta}_{\mathrm{shear}}$ is the relative shear displacement. The quadratic power law of tractions was used as the damage initiation criterion, and the power law of fracture toughness was used as the damage progression criterion.

$$\frac{\langle\tilde{t}_{\mathrm{I}}\rangle^2}{(\tilde{t}_{\mathrm{I}}^c)^2} + \frac{(\tilde{t}_{\mathrm{II}})^2}{(\tilde{t}_{\mathrm{II}}^c)^2} + \frac{(\tilde{t}_{\mathrm{III}})^2}{(\tilde{t}_{\mathrm{III}}^c)^2} = 1, \tag{7}$$

$$\left(\frac{G_{\mathrm{I}}}{G_{\mathrm{I}}^c}\right)^{\alpha} + \left(\frac{G_{\mathrm{II}}}{G_{\mathrm{II}}^c}\right)^{\alpha} + \left(\frac{G_{\mathrm{III}}}{G_{\mathrm{III}}^c}\right)^{\alpha} = 1, \tag{8}$$

where, $\tilde{t}_i^c$ (i = I, II, III) is interlaminar strength of mode i, G_i is the energy release rate of mode i, G_i^c is interlaminar fracture toughness of mode i, and α is power-law exponent of mixed-mode fracture. After the damage initiation criterion was satisfied, the linear softening process of tractions was considered, and the strength and fracture toughness values of modes II and III were assumed to be equal. Using Eqs. (7) and (8), the mixed-mode relative displacement at damage initiation ($\tilde{\delta}^o$) and that at the final failure ($\tilde{\delta}^f$) are obtained using the mixed-mode ratio β as follows.

$$\tilde{\delta}^o = \begin{cases} \tilde{\delta}_{\mathrm{I}}^o \tilde{\delta}_{\mathrm{II}}^o \sqrt{\dfrac{1+\beta^2}{\left(\tilde{\delta}_{\mathrm{II}}^o\right)^2 + \left(\beta\tilde{\delta}_{\mathrm{I}}^o\right)^2}} & (\tilde{\delta}_{\mathrm{I}} > 0) \\ \tilde{\delta}_{\mathrm{II}}^o & (\tilde{\delta}_{\mathrm{I}} \leq 0) \end{cases}, \tag{9}$$

$$\tilde{\delta}^f = \begin{cases} \dfrac{2(1+\beta^2)}{K\tilde{\delta}^o}\left\{\left(\dfrac{1}{G_{\mathrm{I}}^c}\right)^{\alpha} + \left(\dfrac{\beta^2}{G_{\mathrm{II}}^c}\right)^{\alpha}\right\}^{-1/\alpha} & (\tilde{\delta}_{\mathrm{I}} > 0) \\ \tilde{\delta}_{\mathrm{II}}^f & (\tilde{\delta}_{\mathrm{I}} \leq 0) \end{cases}, \tag{10}$$

where, $\tilde{\delta}_i^o$ and $\tilde{\delta}_i^f$ are relative displacements at damage initiation and final failure, respectively, of mode i.

$$\tilde{\delta}_{\mathrm{I}}^o = \frac{t_{\mathrm{I}}^c}{K}, \tilde{\delta}_{\mathrm{II}}^o = \frac{\tilde{t}_{\mathrm{II}}^c}{K} = \frac{\tilde{t}_{\mathrm{III}}^c}{K}, \tilde{\delta}_{\mathrm{I}}^f = \frac{2G_{\mathrm{I}}^c}{\tilde{t}_{\mathrm{I}}^c}, \tilde{\delta}_{\mathrm{II}}^f = \frac{2G_{\mathrm{II}}^c}{\tilde{t}_{\mathrm{II}}^c} = \frac{2G_{\mathrm{III}}^c}{\tilde{t}_{\mathrm{III}}^c}, \beta = \frac{\tilde{\delta}_{\mathrm{shear}}}{\tilde{\delta}_{\mathrm{I}}} \tag{11}$$

The damage variable d is represented as follows.

$$d = \max\left[d^*, \min\left[1, \frac{\tilde{\delta}^f(\tilde{\delta} - \tilde{\delta}^o)}{\tilde{\delta}(\tilde{\delta}^f - \tilde{\delta}^o)}\right]\right], \tag{12}$$

where, (*) denotes the value at the previous time step.

In general, bilinear and exponential softening models are used for the traction and relative displacement relationships in the CZM. However, when employing implicit FEA, these softening models deteriorate convergence [27]. The direct iterative method [28,29], arc length method [30,31], and zig-zag softening law [32,33] can be used to eliminate or mitigate this problem. The direct method always follows a solution with reference to the origin. Therefore, it cannot be applied to cases where an incremental analysis, such as an elastoplastic analysis, is required. The arc length method is useful for tracking solutions with softening behavior; however, it may require the adjustment of various parameters of the coupling force model to obtain a convergent solution in analyses with significant damage propagation and large nonlinearity [31]. The zig-zag softening law [32,33] was adopted in this study because it can be applied to incremental analysis and does not require any parameter adjustment of the CZM. In zig-zag softening law, the tangential stiffness of the softening process is modified to be segmentally positive with respect to the linear softening law as shown in Fig. 5. The fracture energy consumed by the CZM was maintained to be equivalent to the linear softening law.

2.4 CDM

Fiber and matrix damage in the ply were modeled using CDM. For shell elements, the effective compliance ***S*** for transversely isotropic damage material [35] can be expressed as follows:

$$\boldsymbol{S} = \begin{bmatrix} \frac{1}{(1-d_1)E_1} & -\frac{\nu_{12}}{E_1} & 0 & 0 & 0 \\ & \frac{1}{(1-d_2\langle\varepsilon_{22}\rangle/\varepsilon_{22})E_2} & 0 & 0 & 0 \\ & & \frac{1}{(1-d_{12})G_{12}} & 0 & 0 \\ & \text{sym.} & & \frac{1}{(1-d_{23})\kappa G_{23}} & 0 \\ & & & & \frac{1}{(1-d_{13})\kappa G_{12}} \end{bmatrix}, \tag{13}$$

where, E is Young's modulus, ν is Poisson's ratio, G is shear modulus, and subscripts 1, 2, and 3 indicate fiber, transverse, and thickness directions, respectively. Furthermore, κ is shear correction parameter and its value is 5/6 in the case of rectangular cross section, and d_1 and d_2 are damage variables associated with fiber and matrix damage, respectively. The shear damage variables were approximated as follows [36].

$$\frac{1}{1-d_{12}}=\frac{1}{2}\left(\frac{1}{1-d_1}+\frac{1}{1-d_2}\right), \tag{14}$$

$$\frac{1}{1-d_{23}}=\frac{1}{2}\left(\frac{1}{1-d_2}+1\right), \tag{15}$$

$$\frac{1}{1-d_{13}}=\frac{1}{2}\left(\frac{1}{1-d_1}+1\right). \tag{16}$$

The smeared crack model (SCM) was employed to analyze damage progression of fiber damage. The maximum stress criterion was used as the fiber damage initiation criterion.

$$\sigma_{11}=X_+, \tag{17}$$

where, σ_{11} and X_+ denote stress along the fiber direction and longitudinal tensile strength, respectively. The stiffness softening process in the $\sigma_{11}-\varepsilon_{11}$ relationship is assumed to be linear after damage initiation. Using the crack band model [37,38] to reduce mesh dependence, the strain ε_{11}^f at which the element completely loses stiffness can be expressed as follows:

$$\varepsilon_{11}^f=\frac{2G_{f+}^c}{X_+ l_c}, \tag{18}$$

where, G_{f+}^c is the fiber tensile fracture toughness and l_c is the characteristic length [39] with a length dimension to normalize the dissipated energy. The fiber damage variable d_1 can be expressed as follows:

$$d_1=\max\left[d_1^*, \min\left[d_1^{\max}, \frac{\varepsilon_{11}^f(\varepsilon_{11}-\varepsilon_{11}^o)}{\varepsilon_{11}(\varepsilon_{11}^f-\varepsilon_{11}^o)}\right]\right], \tag{19}$$

where, $d_1^{\max}=0.9999$ is the upper limit of the damage variable d_1.

The mixed-mode matrix damage SCM [40] is used to calculate damage variable d_2. The following effective strain ε_e is defined to account for matrix crack propagation in the mixed mode.

$$\varepsilon_e=\sqrt{\langle\varepsilon_{22}\rangle^2+(\gamma_{12})^2+(\gamma_{23})^2}. \tag{20}$$

The effective strain is the strains (ε_{22}, γ_{12}, γ_{23}) contributing to the matrix crack opening and is considered to be a uniaxial strain. The effective stress σ_e paired with ε_e is expressed by the following equation from the equivalence of energy release rate.

$$\sigma_e=\frac{\langle\varepsilon_{22}\rangle\sigma_{22}+2\varepsilon_{12}\sigma_{12}+2\varepsilon_{23}\sigma_{23}}{\varepsilon_e}. \tag{21}$$

The $\sigma_e-\varepsilon_e$ relationship describes the matrix damage evolution by assuming a bilinear law of linear softening after damage initiation. The following quadratic stress criterion is used as the damage initiation criterion.

$$\left(\frac{\langle\sigma_{22}\rangle}{Y_+}\right)^2+\left(\frac{\sigma_{12}}{S_\mathrm{L}}\right)^2+\left(\frac{\sigma_{23}}{S_\mathrm{T}}\right)^2=1, \tag{22}$$

where, Y_+ is transverse tensile strength, S_L is the longitudinal shear strength, and S_T is the transverse shear strength. Using the power law of energy criterion for expressing the damage progression behavior, the mixed-mode fracture toughness G_m^c can be expressed as follows.

$$G_\mathrm{m}^c=\left\{\left(\frac{\lambda_\mathrm{I}}{G_{\mathrm{m}+}^c}\right)^\alpha+\left(\frac{\lambda_\mathrm{II}}{G_\mathrm{mL}^c}\right)^\alpha+\left(\frac{\lambda_\mathrm{III}}{G_\mathrm{mT}^c}\right)^\alpha\right\}^{-\frac{1}{\alpha}}, \tag{23}$$

where,

$$\lambda_\mathrm{I}=\frac{\langle\varepsilon_{22}\rangle\sigma_{22}}{g_\mathrm{m}},\lambda_\mathrm{II}=\frac{2\varepsilon_{12}\sigma_{12}}{g_\mathrm{m}},\lambda_\mathrm{III}=\frac{2\varepsilon_{23}\sigma_{23}}{g_\mathrm{m}}, \tag{24}$$

$$g_\mathrm{m}=\langle\varepsilon_{22}\rangle\sigma_{22}+2\varepsilon_{12}\sigma_{12}+2\varepsilon_{23}\sigma_{23}. \tag{25}$$

$G_{\mathrm{m}+}^c$, G_mL^c, and G_mT^c are the matrix fracture toughness value of modes I, II, and III, respectively. Using crack band model, the effective strain ε_e^f at failure is expressed as follows:

$$\varepsilon_e^f=\frac{2G_\mathrm{m}^c}{\sigma_e^o l_c}, \tag{26}$$

where, σ_e^o is the effective stress when the matrix damage initiation criterion (Eq. (22)) is satisfied. The matrix damage variable d_2 is expressed as follows:

$$d_2=\max\left[d_2^*,\min\left[d_2^\mathrm{max},\frac{\varepsilon_e^f(\varepsilon_e-\varepsilon_e^o)}{\varepsilon_e\left(\varepsilon_e^f-\varepsilon_e^o\right)}\right]\right], \tag{27}$$

where, ε_e^o is effective strain at the matrix damage initiation and $d_2^\mathrm{max}=0.9999$ is the upper limit of damage variable d_2. The zig-zag softening law [32,34] was used when calculating the damage variables d_1 and d_2.

2.5 XFEM

XFEM was used to model displacement discontinuities due to a hole and gaps independently of the finite element mesh. According to partition of unity [41,42], the displacement $\boldsymbol{u}(\boldsymbol{x})$ in the shell element can be approximated as follows.

$$\boldsymbol{u}(\boldsymbol{x}) = \sum_{I=1}^{4} \boldsymbol{N}_{\text{std}}^{I}\left(\boldsymbol{U}_{\text{std}}^{I} + g(\boldsymbol{x})\boldsymbol{U}_{\text{enr}}^{I}\right), \tag{28}$$

where, $g(\boldsymbol{x})$ is the enrichment function that represents the discontinuities of displacement, and $\boldsymbol{U}_{\text{enr}}^{I}$ is the generalized nodal displacement vector added at node I along with the enrichment function.

The gap was modeled as a built-in crack using XFEM. To represent the displacement discontinuity in the vicinity of the crack, the DoF of the nodes in the element through which the crack passes were enriched. This enriched node was defined as a *J*-type node. If shell element has *J*-type nodes, Eq. (28) can be expressed as follows.

$$\boldsymbol{u}(\boldsymbol{x}) = \sum_{I=1}^{4} \boldsymbol{N}_{\text{std}}^{I}\boldsymbol{U}_{\text{std}}^{I} + \sum_{I\in J} \boldsymbol{N}_{\text{std}}^{I} H(\boldsymbol{x})\boldsymbol{U}_{\text{enr}}^{I}, \tag{29}$$

where, J denotes the *J*-type node. The Heaviside function $g(\boldsymbol{x}) = H(\boldsymbol{x})$ was used to account for the crack-induced discontinuities. As shown in Fig. 6, $H(\boldsymbol{x})$ is set to 1 if above the crack line and -1 if below. Each *J*-type node has 10 DoF.

The displacement discontinuity at the free surface is represented by extending the nodal DoF of the elements through which the free surface boundary passes. This enriched node is defined as an *F*-type node. The step function $g(\boldsymbol{x}) = V(\boldsymbol{x})$ was used, where $V(\boldsymbol{x})$ takes the value 1 inside the analysis domain and 0 outside it, as shown in Fig. 6. If shell element has F-type nodes, Eq. (28) is described as follows.

$$\boldsymbol{u}(\boldsymbol{x}) = \sum_{I=1}^{4} \boldsymbol{N}_{\text{std}}^{I}\boldsymbol{U}_{\text{std}}^{I} V(\boldsymbol{x}) \tag{30}$$

As expressed in Eq. (30), the DoF does not increase at the enriched *F*-type nodes.

When both the *J*- and *F*-type nodes exist in an element, the displacement field within the element is expressed using shifting technique [43,44] as follows:

$$\boldsymbol{u}(\boldsymbol{x}) = \left(\sum_{I=1}^{4} \boldsymbol{N}_{\text{std}}^{I}\boldsymbol{U}_{\text{std}}^{I} + \sum_{\text{I}\in\text{J}} \boldsymbol{N}_{\text{std}}^{I}\big(H(\boldsymbol{x}) - H(\boldsymbol{x}^{I})\big)\boldsymbol{U}_{\text{enr}}^{I}\right) V(\boldsymbol{x}), \tag{31}$$

where, $\boldsymbol{x}^{I}$ is the nodal position. The displacement $\boldsymbol{u}(\boldsymbol{x})$ of an enriched element is calculated using Eq. (31), which implies that the displacement field and nodal displacements coincide at J nodes. To represent the load transfer [45,46] between the shell layers and the cohesive elements in the vicinity of the crack, the crack is also inserted into the cohesive elements between the shell layers located above or below the crack using Eq. (31).

The CZM [26] presented in Section 2.3 is applied between crack surfaces of XFEM to consider the opening and closing of the gap filled with resin. The model wherein CZM was inserted on the crack surface of XFEM is labeled as XFEM_CZM. Two integration points are placed on the crack line in the element as evaluation points for the crack opening displacement. In the XFEM_CZM, the XFEM crack surface was bounded by the CZM. Therefore, crack growth can be predicted as the crack opens in accordance with the CZM, as the load increases, and the crack length can be predicted. This method requires specification of the crack propagation direction in advance.

Gaussian integration cannot be applied directly for calculating the element stiffness matrix when discontinuous functions are expanded in XFEM. Therefore, the element was divided into several sub-elements and the Gaussian integral was applied after ensuring that no discontinuities are included within the sub-elements. Fig. 7 shows the element partitioning pattern used in this study. The element is divided such that the minimum number of triangles or squares was obtained based on the crack line.

3. Verification

To verify the developed model, the OHT analysis of IM7/8552 $[45_4/90_4/\text{-}45_4/0_4]_s$ laminate without gaps was conducted and compared with experimental results reported by Hallett et al. [22] and Song et. al. [23]. The material properties considered in this study are listed in Table 1.

The finite element model of OHT specimen of IM7/8552 $[45_4/90_4/\text{-}45_4/0_4]_s$ laminate [22] is shown in Fig. 8. The symmetric boundary condition is applied on the mid-plane of the laminate, and half of the laminate is modelled. The laminate length, width, and half thickness are L = 63.5 mm, W = 15.875 mm, and t = 2 mm, respectively. The circular hole diameter is d = 3.175 mm. Four angle plies of the same type are represented by a single shell layer. The enforced displacement along x-axis is applied on $x = L$, and the x-direction displacement is fixed on $x = 0$. At the grip ends, the transverse displacement v along y-axis is fixed in the width direction at both ends to account for the effect of gripping.

Three different models (Standard, Aligned, and SCM_DCM (the model using the SCM and XFEM_CZM of the discrete crack model)) with different mesh patterns were used, as shown in Fig. 9. The meshes for the Standared and Aligned models were generated using the commercial software ABAQUS CAE [47]. Aligned meshes were generated using the partitioning and local mesh seed specification capabilities in ABAQUS CAE based on the mesh pattern in the literature [22]. The Standard model has only square mesh and the circular hole is modeled using XFEM. Mesh size is approximately 0.35 mm. The total number of nodes and elements are 33,488 and 32,580, respectively. The dependence of damage propagation by CDM on the mesh has been pointed out in previous studies [48–50]. To investigate the mesh dependency of the CDM, the Aligned and SCM_DCM models were considered. The Aligned model has the mesh pattern where the crack propagation direction coincides with mesh direction. Based on suggestions in [22], the hole shape was adjusted to prevent distortion of the mesh shape. The total number of nodes and elements are 31,792 and 30,912, respectively. The SCM_DCM model has the same square mesh as the Standard model and introduces XFEM_CZM to represent diagonally oriented cracks in 45 and -45° layers. Two cracks are placed in each of the 45° and -45° layers in the fiber direction for the entire width and in contact with the circular hole edge. The increase in the total DoF by using XFEM_CZM, compared to the Standard model, is approximately 2%. Static implicit incremental FEA (0.0045 mm displacement increment) is performed using three models.

The FEA and experimental [22,51] results of load-displacement relationship are shown in Fig. 10. The initial stiffness values of FEA results obtained for the three models are slightly higher than that of the experimental results. This may be due to plasticity of the off-axis CFRP plies. However, the discrepancy between experiments and numerical results is small as shown in Fig. 10. A significant first load drop was observed at approximately 0.34 mm in the experimental results. This load drop is caused by the significant delamination propagation at the −45°/0° ply interface [22]. The overall load–displacement diagrams obtained from three models are in general agreement with the experimental data. For a more detailed comparison of the three models, the matrix damage and delamination distributions immediately after the first load drop will be discussed.

The matrix damage distributions of each ply immediately after the first load drop predicted by three models are shown in Fig. 11, and the X-ray image [22] is shown in Fig. 12 (a) for comparison. From Fig. 12 (a), major cracks, which are several long cracks extending from the circular hole edge, and diffused cracks, which are short and consist of multiple cracks, were observed in the experiments. Major cracks promote delamination due to stress concentration at the crack tip, while diffused cracks cause localized stiffness softening. In the Standard model, the major cracks in the 0° plies and the diffused cracks in the 90° plies are well represented, as shown in Fig. 11, but the major cracks in the ±45° plies are absent. This is due to the difference between the mesh direction and the direction of crack propagation. Moreover, the accuracy of crack growth prediction can be improved when the mesh direction coincides with the crack direction [49,50]. On the other hand, diffused cracks in the 90° layer and major cracks in the other layers are well represented in the Aligned and SCM_DCM models. Although the mesh direction and the crack propagation direction are the same in Aligned mesh, the generation of such a mesh is empirical and labor-intensive. The SCM_DCM model has a simple square mesh, but the introduction of the XFEM_CZM crack model in the ±45° plies predicts experimental crack initiation and propagation as accurately as the Aligned model.

Fig. 13 shows the predicted delamination distributions after the first load drop. The stress concentration at the major crack tip promotes delamination. The X-lay images in each interface of Fig. 12 (b) shows that the positions of the major crack tips in the 45°, -45°, and 0° layers coincide with the delamination front. As shown in Fig. 13, the Standard model incorrectly predicted the ±45° major crack, resulting in a delamination distribution that differed from the experimental observation. On the other hand, the Aligned and SCM_DCM models correctly predicted the major cracks and their results are in qualitative agreement with the experiments.

These results indicate that Aligned and SCM_DCM models are able to follow the damage propagation behavior of OHT laminates. One way to improve the prediction accuracy of the damage distribution in the standard model is to use nonlocal damage theory [48,52]. Nonlocal damage theory can be used to mitigate the mesh dependence of the SCM. However, incorporating nonlocal damage theory into an implicit FEA can lead to a deterioration in convergence [48]. The Aligned model moderates the mesh dependence CDM by generating the mesh in the direction of crack propagation. Some studies [50,53] have attempted OHT analyses based on the same concept, but complex meshing is unavoidable. Furthermore, the finite element mesh of the Aligned model must be changed empirically as the stacking configuration changes. However, to improve the consistency of the analysis, SCM_DCM allows the same square mesh. Therefore, the SCM_DCM model with a simple square mesh using both CDM and XFEM_CZM is a suitable approach for damage propagation analysis of CFRP laminates with a hole.

4. Strength prediction of a quasi-isotropic laminate with gaps

4.1 Experiment

The OHT specimen of quasi-isotropic CFRP laminate with gaps is shown in Fig. 14. The material is T800S/3900-2B (Toray Industries) and stacking sequence is $[45/90/\text{-}45/0]_{2s}$. The specimen dimensions are length = 350 mm, width = 100 mm, thickness = 3.04 mm, and hole diameter = 25 mm. The gap perpendicular to the load is made manually at the center of the circular hole in all 90° plies. The specimen had four gaps, all of which were in the same position with respect to the through-thickness direction. The gap width before curing of CFRP prepreg is 2 mm. The CFRP laminate is autoclaved, and a cowl plate is used at the curing process of the prepreg to minimize the fiber waviness. The laminates without gaps were also prepared to compare the tensile strength of specimens with or without gaps. The OHT tests were conducted using hydraulic testing machine to obtain the load–strain relationships, tensile strengths, and photographs of failure of OHT specimens. The strain values used for comparison with the analysis were the averaged values of the strain gauges attached to the S1, S2, S3, and S4 positions, as shown in Fig. 14. Fig. 15 shows an edge view of a specimen with gaps near the hole. After curing of the CFRP, the width of each gap was approximately 1 mm. The gap positions moved slightly because of resin flow. As shown in Fig. 15, the plies near the gap were almost straight with no waviness, suggesting that the effect of fiber waviness on the strength of the specimens with gaps was very small. The obtained load–strain relationships and photographs of failure of OHT specimens with or without gaps are shown in Figs. 16 and 17, respectively.

4.2 Analytical results and discussion

The proposed model is compared with experimental results on ultimate tensile strength and damage progression at final failure in open hole T800S/3900-2B $[45/90/\text{-}45/0]_{2s}$ laminates with manually-introduced gaps. The material properties used in this study are shown in Table 1.

The OHT analysis model for the T800S/3900-2B $[45/90/\text{-}45/0]_{2s}$ specimen with gaps in 90° plies is shown in Fig. 18. The symmetric boundary condition was applied on the mid-plane of the laminate, and half of the laminate was modeled. Each ply was modeled with one shell layer. The circular holes were modeled by XFEM. In addition to ±45° major cracks, the gap is modeled using the XFEM_CZM model to consider resin rich region at the gap. The material properties of the CZM at the gaps are the same as those of the delamination because resin rich region exists at the interfaces. The gap was placed such that it passed through the center of the elements. In addition, analysis of same laminate but without gaps was conducted as a reference. The square meshes sized approximately 1 mm were used in each ply. The total number of nodes and that of elements were 161,600 and 159,200, respectively. The enforced displacement along x-axis was applied on $x = L$, while the x-direction displacement was fixed on $x = 0$. At the grip ends, the transverse displacement v along y-axis is fixed in the width direction at both ends to account for the effect of the gripping. The strain increment was set to 0.01%.

Fig. 16 shows the analytical and experimental load–strain diagrams with and without gaps in 90° plies. The strain in the analysis is calculated by dividing the applied displacement by the longitudinal length. Comparing the results of FEA and experiments with gaps, the analysis shows slightly higher stiffness, but the overall load–strain behavior up to failure agrees well with the experiment despite the simplified modeling. Table 2 shows the tensile strengths of the experimental and FEA results. The analysis shows a slightly lower strength with and without gaps than that of experiments but agrees well with the experiment with maximum percentage error of 5.5% for specimens with and without gaps. Both the experimental and analytical strength values for specimens with gaps are slightly larger than for those without gaps. Therefore, we concluded that the gap has some effect on the strength.

To investigate the effect of gap on tensile strength, the stress distribution in the 0° ply that is the load–bearing layer and the matrix damage distribution in the 90° ply with gaps are compared with those without gaps. Fig. 19 shows the axial stress distribution near the circular hole in the fourth 0° layer from the surface (Ply 4 in Fig. 14 (a)) of the laminate with and without gap immediately before final failure. Note that the failure strain in specimen with gaps is different from that in its counterpart without gaps. The stress concentration at the circular hole edge of the 0° ply is reduced in the vicinity of the gap. Similar phenomena were observed in the other 0° plies. Fig. 20 shows the distribution of the matrix damage variable d_2 for the second 90° ply from the surface (Ply 2 in Fig. 14 (a)) with and without a gap immediately before and after final failure. In the absence of the gap, the cracks propagate extensively in the 90° ply, whereas in the presence of the gap, the cracks are confined to the gap, resulting in a narrower crack zone. As shown in Fig. 17, the wide failure zone is observed for the specimen without gaps while a rectilinear crack zone appeared in the specimen with gaps. Therefore, the predicted matrix crack distributions qualitatively agreed with the experimental results obtained for at final failure. As shown in Fig. 20 (b), the gap is slightly opened at the edge of the circular hole. Therefore, the gap opening can reduce the stress concentration at the hole, resulting in higher strength of composite laminate with gaps than that without gaps.

Figs. 21 and 22 show the axial strain distribution of 90° ply of Ply 2 and Ply 6 in the laminate (a) without or (b) with gaps in 90° plies at 0.69% applied strain, respectively. In the case without a gap, the axial strain was large over a wide area, including the edge of the hole, because of the stress concentration caused by the hole. By contrast, in the case with a gap, the axial strain at the edge of the circular hole just above the gap was small, and the strain was large around the edge. Because of the stress redistribution caused by the gap opening, there were fewer matrix cracks at the edge of the circular hole. Therefore, opening the gap did not increase the stress concentration in the 0° ply, and was not expected to cause premature failure. In the stress distribution of the 0° ply as shown in Fig. 19, the maximum stress value as well as the stress at the edge of the circular hole is smaller in the analysis with the gaps than in the case without gaps.

The percentages of the strength change were 1.68% and 4.11% in the experiment and in the analysis, respectively. The small percentage strength change in the experiment can be attributed to the change in the gap position before and after the curing. As shown in Fig. 15, the gap position after curing changed slightly owing to the resin flow. A slight shift of each gap from the circular hole edge reduced the effect of the gap on stress concentration. Therefore, the rate of change in strength in the experiment was small.

5. Conclusion

This study developed the ply-by-ply shell layer model to explore the impact of a gap on the damage progression and strength of composite laminate using simplified modeling to reduce computational costs. The gap is modeled using the XFEM_CZM model combining XFEM and CZM to simplify the finite element mesh and consider resin rich region at the gap. The same mesh can be used for various gap geometries, which saves pre-processing and improves the consistency of the analysis process.

To verify the proposed model, the OHT analysis of IM7/8552 $[45_4/90_4/\text{-}45_4/0_4]_s$ laminate without gaps was conducted and compared with experimental results. The matrix damage and delamination evolutions were successfully reproduced using the simplified square mesh using both the XFEM_CZM model for the major cracks in the ±45° plies and CDM for diffused cracks.

OHT analysis was performed on a specimen of T800S/3900-2B $[45/90/\text{-}45/0]_{2s}$ laminate with a gap in each 90° ply to investigate the effect of the gap on tensile strength and matrix damage distribution. Although the analytical results showed slightly high stiffness values than those obtained experimentally, the overall load–strain behavior up to final failure agreed well with the experimental results despite the simplified modeling. Both the experimental and analytical strengths with gaps are slightly higher than those without gaps. It is one of the causes that the gap opening reduced the stress concentration at the hole, resulting in higher strength of composite laminate with gaps than that of its counterpart without gaps.

Appendix A Bending analysis of the cantilever beams

Shear locking generally occurs in shell elements as their thickness decreases. A bending analysis of the cantilever beams confirmed the ability of the MITC shell elements to avoid shear locking. The bending accuracy was compared between the MITC shell element and the shell element without the out-of-plane shear strain redefinition. Cantilever beam bending analysis was performed on a 150 mm long and 20 mm wide plate. The left end of the beam was completely fixed, and the right end was subjected to a 5 mm downward forced displacement as a boundary condition. The plate thickness was varied from 1 to 10 mm, and the loads at the point of forced displacement were calculated and compared with beam theory. Fig. A.1 presents a comparison of the loads for pure bending of varying thicknesses. The vertical axis was normalized by the load using the theoretical solution of beam theory, and the horizontal axis was normalized by the thickness of the beam. As shown in Fig. A.1, the load of the shell element without the out-of-plane shear strain redefinition (labeled as No interpolation) was overestimated because of shear locking as the plate thickness became thinner than the longitudinal length. However, the MITC shell element (labeled as MITC) shows no shear locking, even under thin-wall conditions, and the solution is almost the same as the theoretical solution.

Appendix B Double cantilever beam and end notched flexure analyses

The validity of the MITC shell element and CZM was verified by performing 3-D analyses of the double cantilever beam (DCB) and end notched flexure (ENF) tests and comparing them to theoretical solutions based on the modified beam theory [54,55]. A $[0]_2$ CFRP laminate was used in the analysis. The dimensions and boundary conditions of the numerical model for the DCB analysis are shown in Fig. B.1 (a). The specimen was 150 mm long, 20 mm wide, 3.1 mm thick and had a pre-crack length of 35 mm. In the finite element model, the specimen was represented by two shell layers with the CZM inserted between the layers. The mesh size of each shell is a square mesh of 0.5 mm (40 sections in the width direction and 300 sections in the longitudinal direction) with 24,681 total nodes and 24,000 total elements. The dimensions and boundary conditions of the numerical model for the ENF analysis are shown in Fig. B.1 (b). The specimen was 150 mm long, 1 mm wide, 3.1 mm thick and had a pre-crack length of 35 mm. In the finite element model, the specimen was represented by two shell layers with the CZM inserted between the layers. Because contact occurred at the pre-crack region in the ENF analysis, a contact element based on the penalty method was introduced on the pre-crack surface to account for the contact. The mesh size for each shell was a square mesh of 0.2 mm (5 sections in the width direction and 750 sections in the longitudinal direction) with 9,012 total nodes and 7,500 total elements. These two models were analyzed for delamination propagation. Their material properties and parameters are presented in Table B.1. Fig. B.2 shows the relationship between the crack opening displacement, load point displacement, and load obtained from the in-house FEA code and modified beam theory [54,55]. The results obtained using the in-house FEA code were generally consistent with the theoretical solution. Therefore, the correct traction acts on the cohesive elements between shell elements.

Acknowledgements

This research was supported by the Council for Science, Technology, and Innovation (CSTI) and the Cross-Ministerial Strategic Innovation Promotion Program (SIP), ''Materials Integration for Revolutionary Design System of Structural Materials'' (Funding agency: JST). The authors thank Mr. Abe, Mr. Oka and Mr. Kashiwagi (Mitsubishi Heavy Industries) for providing experimental data and discussion.

References

[1] Brasington A, Sacco C, Halbritter J, Wehbe R, Harik R. Automated fiber placement: A review of history, current technologies, and future paths forward. Compos Part C Open Access 2021;6:100182. https://doi.org/10.1016/j.jcomc.2021.100182.

[2] Lukaszewicz DHJA, Ward C, Potter KD. The engineering aspects of automated prepreg layup: History, present and future. Compos Part B Eng 2012;43:997–1009. https://doi.org/10.1016/j.compositesb.2011.12.003.

[3] Esposito L, Cutolo A, Barile M, Lecce L, Mensitieri G, Sacco E, et al. Topology optimization-guided stiffening of composites realized through Automated Fiber Placement. Compos Part B Eng 2019;164:309–23. https://doi.org/10.1016/j.compositesb.2018.11.032.

[4] Denkena B, Schmidt C, Weber P. Automated Fiber Placement Head for Manufacturing of Innovative Aerospace Stiffening Structures. Procedia Manuf 2016;6:96–104. https://doi.org/10.1016/j.promfg.2016.11.013.

[5] Heinecke F, Willberg C. Manufacturing-induced imperfections in composite parts manufactured via automated fiber placement. J Compos Sci 2019;3:1–24. https://doi.org/10.3390/jcs3020056.

[6] Simacek P, Niknafs Kermani N, Gargitter V, Advani SG. Role of resin percolation in gap filling mechanisms during the thin ply thermosetting automated tape placement process. Compos Part A Appl Sci Manuf 2022;152:106677. https://doi.org/10.1016/j.compositesa.2021.106677.

[7] Nardi D, Abouhamzeh M, Leonard R, Sinke J. Experimental Investigation of the Effects of Pre-Preg Gaps for the Automated Production of Fiber Metal Laminates. Proc. 18th Eur. Conf. Compos. Mater., 2018.

[8] Woigk W, Hallett SR, Jones MI, Kuhtz M, Hornig A, Gude M. Experimental investigation of the effect of defects in Automated Fibre Placement produced composite laminates. Compos Struct 2018;201:1004–17. https://doi.org/10.1016/j.compstruct.2018.06.078.

[9] Nguyen MH, Vijayachandran AA, Davidson P, Call D, Lee D, Waas AM. Effect of automated fiber placement (AFP) manufacturing signature on mechanical performance of composite structures. Compos Struct 2019;228:111335. https://doi.org/10.1016/j.compstruct.2019.111335.

[10] Nguyen MH, Vijayachandran AA, Davidson P, Call D, Lee D, Waas AM. Effect of automated fiber placement (AFP) manufacturing signature on mechanical performance. AIAA Scitech 2019 Forum 2019. https://doi.org/10.2514/6.2019-0516.

[11] Abouhamzeh M, Nardi D, Leonard R, Sinke J. Effect of prepreg gaps and overlaps on mechanical

properties of fibre metal laminates. Compos Part A Appl Sci Manuf 2018;114:258–68. https://doi.org/10.1016/j.compositesa.2018.08.028.

[12] Croft K, Lessard L, Pasini D, Hojjati M, Chen J, Yousefpour A. Experimental study of the effect of automated fiber placement induced defects on performance of composite laminates. Compos Part A Appl Sci Manuf 2011;42:484–91. https://doi.org/10.1016/j.compositesa.2011.01.007.

[13] Nardi D, Abouhamzeh M, Leonard R, Sinke J. Detection and Evaluation of Pre-Preg Gaps and Overlaps in Glare Laminates. Appl Compos Mater 2018;25:1491–507. https://doi.org/10.1007/s10443-018-9679-z.

[14] Lan M, Cartié D, Davies P, Baley C. Microstructure and tensile properties of carbon–epoxy laminates produced by automated fibre placement: Influence of a caul plate on the effects of gap and overlap embedded defects. Compos Part A Appl Sci Manuf 2015;78:124–34. https://doi.org/10.1016/j.compositesa.2015.07.023.

[15] Del Rossi D, Cadran V, Thakur P, Palardy-Sim M, Lapalme M, Lessard L. Experimental investigation of the effect of half gap/half overlap defects on the strength of composite structures fabricated using automated fibre placement (AFP). Compos Part A Appl Sci Manuf 2021;150. https://doi.org/10.1016/j.compositesa.2021.106610.

[16] Lan M, Cartié D, Davies P, Baley C. Influence of embedded gap and overlap fiber placement defects on the microstructure and shear and compression properties of carbon–epoxy laminates. Compos Part A Appl Sci Manuf 2016;82:198–207. https://doi.org/10.1016/j.compositesa.2015.12.007.

[17] Marouene A, Legay P, Boukhili R. Experimental and numerical investigation on the open-hole compressive strength of AFP composites containing gaps and overlaps. J Compos Mater 2017;51:3631–46. https://doi.org/10.1177/0021998317690917.

[18] Nartey M, Zhang T, Gong B, Wang J, Peng S, Wang H, et al. Understanding the impact of fibre wrinkle architectures on composite laminates through tailored gaps and overlaps. Compos Part B Eng

2020;196:108097. https://doi.org/10.1016/j.compositesb.2020.108097.

[19] Li X, Hallett SR, Wisnom MR. Modelling the effect of gaps and overlaps in automated fibre placement (AFP)-manufactured laminates. Sci Eng Compos Mater 2015;22:115–29. https://doi.org/10.1515/secm-2013-0322.

[20] Falcó O, Lopes CS, Naya F, Sket F, Maimí P, Mayugo JA. Modelling and simulation of tow-drop effects arising from the manufacturing of steered-fibre composites. Compos Part A Appl Sci Manuf 2017;93:59–71. https://doi.org/10.1016/j.compositesa.2016.11.015.

[21] Nguyen MH, Davidson P, Waas AM. Experimental and numerical study on the tensile failure behavior of toughened-interlayer composite laminates with automated fiber placement (AFP) induced gap and overlap defects. Int J Mater Form 2021;14:105–19. https://doi.org/10.1007/s12289-020-01581-w.

[22] Hallett SR, Green BG, Jiang WG, Wisnom MR. An experimental and numerical investigation into the damage mechanisms in notched composites. Compos Part A Appl Sci Manuf 2009;40:613–24. https://doi.org/10.1016/j.compositesa.2009.02.021.

[23] Song K, Li Y, Rose CA. Continuum damage mechanics models for the analysis of progressive failure in open-hole tension laminates. Collect Tech Pap - AIAA/ASME/ASCE/AHS/ASC Struct Struct Dyn Mater Conf 2011:1–18. https://doi.org/10.2514/6.2011-1861.

[24] Dvorkin EN, Bathe KJ. A continuum mechanics based four-node shell element for general nonlinear analysis. Eng Comput 1984;1:77–88. https://doi.org/10.1108/eb023562.

[25] Bathe K -J, Dvorkin EN. A formulation of general shell elements—the use of mixed interpolation of tensorial components. Int J Numer Methods Eng 1986;22:697–722. https://doi.org/10.1002/nme.1620220312.

[26] Camanho PP, Davila CG, de Moura MF. Numerical Simulation of Mixed-Mode Progressive Delamination in Composite Materials. J Compos Mater 2003;37:1415–38. https://doi.org/10.1177/0021998303034505.

[27] Crisfield MA, Jelenic G, Mi Y, Zhong HG, Fan Z. Some aspects of the non-linear finite element method. Finite Elem Anal Des 1997;27:19–40. https://doi.org/10.1016/S0168-874X(97)00004-8.

[28] Yashiro S, Takeda N, Okabe T, Sekine H. A new approach to predicting multiple damage states in composite laminates with embedded FBG sensors. Compos Sci Technol 2005;65:659–67. https://doi.org/10.1016/j.compscitech.2004.09.022.

[29] Yoshimura A, Yashiro S, Okabe T, Takeda N. Characterization of tensile damage progress in stitched CFRP laminates. Adv Compos Mater Off J Japan Soc Compos Mater 2007;16:223–44. https://doi.org/10.1163/156855107781393740.

[30] van der Meer FP, Sluys LJ. Mesh-independent modeling of both distributed and discrete matrix cracking in interaction with delamination in composites. Eng Fract Mech 2010;77:719–35. https://doi.org/10.1016/j.engfracmech.2009.11.010.

[31] Van Der Meer FP, Sluys LJ, Hallett SR, Wisnom MR. Computational modeling of complex failure mechanisms in laminates. J Compos Mater 2012;46:603–23. https://doi.org/10.1177/0021998311410473.

[32] Ridha M, Wang CH, Chen BY, Tay TE. Modelling complex progressive failure in notched composite laminates with varying sizes and stacking sequences. Compos Part A Appl Sci Manuf 2014;58:16–23. https://doi.org/10.1016/j.compositesa.2013.11.012.

[33] Tay TE, Sun XS, Tan VBC. Recent efforts toward modeling interactions of matrix cracks and delaminations: An integrated XFEM-CE approach. Adv Compos Mater 2014;23:391–408. https://doi.org/10.1080/09243046.2014.915092.

[34] Graça-E-Costa R, Alfaiate J, Dias-Da-Costa D, Sluys LJ. A non-iterative approach for the modelling of quasi-brittle materials. Int J Fract 2012;178:281–98. https://doi.org/10.1007/s10704-012-9768-1.

[35] Lopes CS, Camanho PP, Gürdal Z, Maimí P, González E V. Low-velocity impact damage on

dispersed stacking sequence laminates. Part II: Numerical simulations. Compos Sci Technol 2009;69:937–47. https://doi.org/10.1016/j.compscitech.2009.02.015.

[36] Chow CL, Lu TJ. On evolution laws of anisotropic damage. Eng Fract Mech 1989;34:679–701. https://doi.org/10.1016/0013-7944(89)90130-6.

[37] Bažant ZP, Oh BH. Crack band theory for fracture of concrete. Matériaux Constr 1983;16:155–77. https://doi.org/10.1007/BF02486267.

[38] Oliver J. A consistent characteristic length for smeared cracking models. Int J Numer Methods Eng 1989;28:461–74. https://doi.org/10.1002/nme.1620280214.

[39] Pinho ST, Iannucci L, Robinson P. Physically based failure models and criteria for laminated fibre-reinforced composites with emphasis on fibre kinking. Part II: FE implementation. Compos Part A Appl Sci Manuf 2006;37:766–77. https://doi.org/10.1016/j.compositesa.2005.06.008.

[40] Lu X, Ridha M, Tan VBC, Tay TE. Adaptive discrete-smeared crack (A-DiSC) model for multi-scale progressive damage in composites. Compos Part A Appl Sci Manuf 2019;125. https://doi.org/10.1016/j.compositesa.2019.105513.

[41] Melenk JM, Babuška I. The partition of unity finite element method: Basic theory and applications. Comput Methods Appl Mech Eng 1996;139:289–314. https://doi.org/10.1016/S0045-7825(96)01087-0.

[42] Babuška I, Melenk JM. The partition of unity method. Int J Numer Methods Eng 1997;40:727–58. https://doi.org/10.1002/(SICI)1097-0207(19970228)40:4<727::AID-NME86>3.0.CO;2-N.

[43] Fathi F, Chen L, de Borst R. Extended isogeometric analysis for cohesive fracture. Int J Numer Methods Eng 2020;121:4584–613. https://doi.org/10.1002/nme.6453.

[44] Fries T. A corrected XFEM approximation without problems in blending elements. Int J Numer Methods Eng 2008;75:503–32. https://doi.org/10.1002/nme.2259.

[45] Lu X, Chen BY, Tan VBC, Tay TE. A separable cohesive element for modelling coupled failure

in laminated composite materials. Compos Part A Appl Sci Manuf 2018;107:387–98. https://doi.org/10.1016/j.compositesa.2018.01.014.

[46] Fang XJ, Yang QD, Cox BN, Zhou ZQ. An augmented cohesive zone element for arbitrary crack coalescence and bifurcation in heterogeneous materials. Int J Numer Methods Eng 2011;88:841–61. https://doi.org/10.1002/nme.3200.

[47] ABAQUS. 6.13 Documentation. Dassault Syst Simulia Corp 2013.

[48] Bažant ZP, Jirásek M. Nonlocal Integral Formulations of Plasticity and Damage: Survey of Progress. Perspect Civ Eng Commem 150th Anniv Am Soc Civ Eng 2003;128:21–51.

[49] Millen SLJ, Ullah Z, Falzon BG. On the importance of finite element mesh alignment along the fibre direction for modelling damage in fibre-reinforced polymer composite laminates. Compos Struct 2021;278:114694. https://doi.org/10.1016/j.compstruct.2021.114694.

[50] Falcó O, Ávila RL, Tijs B, Lopes CS. Modelling and simulation methodology for unidirectional composite laminates in a Virtual Test Lab framework. Compos Struct 2018;190:137–59. https://doi.org/10.1016/j.compstruct.2018.02.016.

[51] Lu X, Ridha M, Tan VBC, Tay TE. Adaptive discrete-smeared crack (A-DiSC) model for multi-scale progressive damage in composites. Compos Part A Appl Sci Manuf 2019;125:105513. https://doi.org/10.1016/j.compositesa.2019.105513.

[52] Bažant ZP, Pijaudier-Cabot G. Nonlocal continuum damage, localization instability and convergence. J Appl Mech Trans ASME 1988;55:287–93. https://doi.org/10.1115/1.3173674.

[53] Nguyen MH, Waas AM. A novel mode-dependent and probabilistic semi-discrete damage model for progressive failure analysis of composite laminates - Part I: Meshing strategy and mixed-mode law. Compos Part C Open Access 2020;3:100073. https://doi.org/10.1016/j.jcomc.2020.100073.

[54] Mi Y, Crisfield MA, Davies GAO, Hellweg HB. Progressive Delamination Using Interface Elements. J Compos Mater 1998;32:1246–72. https://doi.org/10.1177/002199839803201401.

[55] Reeder JR, Demarco K, Whitley KS. The use of doubler reinforcement in delamination toughness testing. Compos Part A Appl Sci Manuf 2004;35:1337–44. https://doi.org/10.1016/j.compositesa.2004.02.021.

[56] Morimoto T, Sugimoto S, Katoh H, Hara E, Yasuoka T, Iwahori Y, et al. JAXA advanced composites database, JAXA research and development memorandum (in Japanese). Tech Rep JAXA-RM-14-004, ISSN 1349-1121 2015.

[57] Higuchi R, Warabi S, Yoshimura A, Nagashima T, Yokozeki T, Okabe T. Experimental and numerical study on progressive damage and failure in composite laminates during open-hole compression tests. Compos Part A Appl Sci Manuf 2021;145:106300. https://doi.org/10.1016/j.compositesa.2021.106300.

[58] Harper PW, Hallett SR. Cohesive zone length in numerical simulations of composite delamination. Eng Fract Mech 2008;75:4774–92. https://doi.org/10.1016/j.engfracmech.2008.06.004.

CRediT authorship contribution statement

S. Onodera: Methodology, Software, Validation, Formal analysis, Data Curation, Writing - Original Draft, Writing - Review & Editing, Visualization, Project administration. **K. Kawahara:** Software, Validation, Formal analysis, Investigation, Visualization. **S. Yashiro:** Conceptualization, Methodology, Writing - Review & Editing, Visualization, Project administration, Supervision, Funding acquisition.

Declaration of conflicting interests

The author(s) declared no potential conflicts of interest with respect to the research, authorship, and/or publication of this article.

Data availability

Data will be made available on request.

Tables and Figures

Table 1 Material properties of IM7/8552 [51] and T800S/3900-2B [56,57].

Property	IM7/8552	T800S/3900-2B
Longitudinal Young's modulus E_1 (GPa)	161	153
Transverse Young's modulus E_2 (GPa)	11.4	8.0
In-Plane shear modulus G_{12} (GPa)	5.17	4.03
Out-of-Plane shear modulus G_{23} (GPa)	3.98	2.75
In-Plane Poisson's ratio ν_{12}	0.32	0.34
Out-of-Plane Poisson's ratio ν_{23}	0.43	0.45
Longitudinal tensile strength X_+ (GPa)	2806	3100
Transverse tensile strength Y_+ (GPa)	60	66.9
Longitudinal shear strength S_L (GPa)	90	118
Transverse shear strength S_T (GPa)	90	118
Fiber tensile fracture toughness G_{f+}^c (N/mm)	112.7	193.3
Mode I matrix tensile fracture toughness $G_{\mathrm{m}+}^c$ (N/mm)	0.297	0.54
Mode II longitudinal matrix fracture toughness G_{mL}^c (N/mm)	0.631	1.64
Mode III transverse matrix fracture toughness G_{mT}^c(N/mm)	0.631	1.64
Mode I interlaminar tensile strength $\tilde{t}_\mathrm{I}^c$ (MPa)	30	66.9
Mode II interlaminar shear strength $\tilde{t}_\mathrm{II}^c$ (MPa)	45	118
Mode III interlaminar shear strength $\tilde{t}_\mathrm{III}^c$ (MPa)	45	118
Mode I interlaminar fracture toughness G_I^c (N/mm)	0.293	0.54
Mode II interlaminar fracture toughness G_II^c (N/mm)	0.631	1.64
Mode III interlaminar fracture toughness G_III^c (N/mm)	0.631	1.64
Power-law exponent of mixed-mode fracture α	1.0	1.0
Penalty stiffness K ($\mathrm{N/mm^3}$)	10^5	10^6

Table 2 OHT strength of experimental and FEA results.

	without gap (kN)	with gap (kN)
Experiment	120.29	122.34
FEA	113.70	118.44
Relative error	5.48 %	3.19 %

Table B.1 Material properties of CFRP for DCB and ENF analyses [58].

Longitudinal Young's modulus E_1 (GPa)	120
Transverse Young's modulus E_2 (GPa)	10.5
In-Plane shear modulus G_{12} (GPa)	5.25
Out-of-Plane shear modulus G_{23} (GPa)	3.98
In-Plane Poisson's ratio ν_{12}	0.3
Out-of-Plane Poisson's ratio ν_{23}	0.51
Mode I interlaminar tensile strength $\tilde{t}_{\mathrm{I}}^{c}$ (MPa)	30
Mode II interlaminar shear strength $\tilde{t}_{\mathrm{II}}^{c}$ (MPa)	60
Mode III interlaminar shear strength $\tilde{t}_{\mathrm{III}}^{c}$ (MPa)	60
Mode I interlaminar fracture toughness G_{I}^{c} (N/mm)	0.26
Mode II interlaminar fracture toughness G_{II}^{c} (N/mm)	1.002
Mode III interlaminar fracture toughness G_{III}^{c} (N/mm)	1.002
Power-law exponent of mixed-mode fracture α	1.0
Penalty stiffness K (N/mm^3)	10^6

Fig. 1. Schematic figure of (a) gap and (b) overlap.

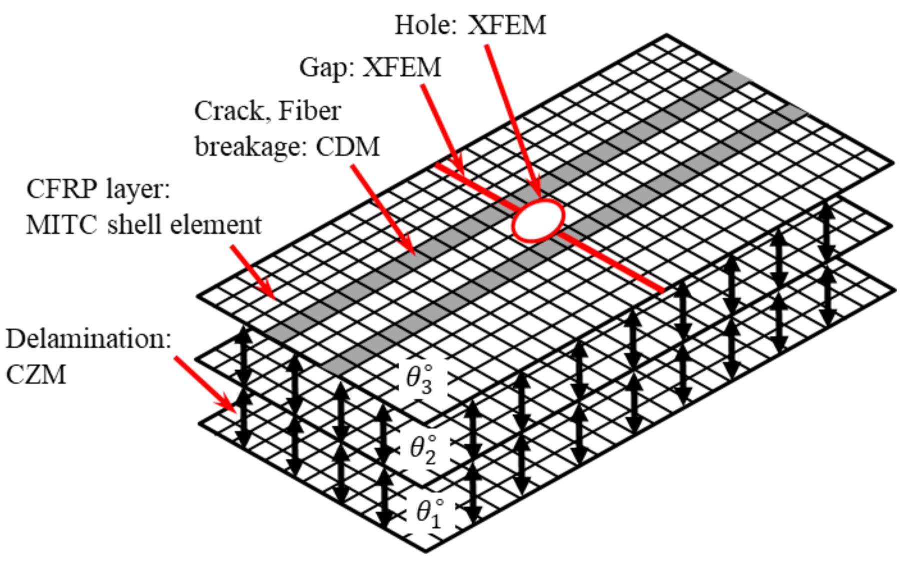

Fig. 2. Schematic figure of ply-by-ply shell layer model.

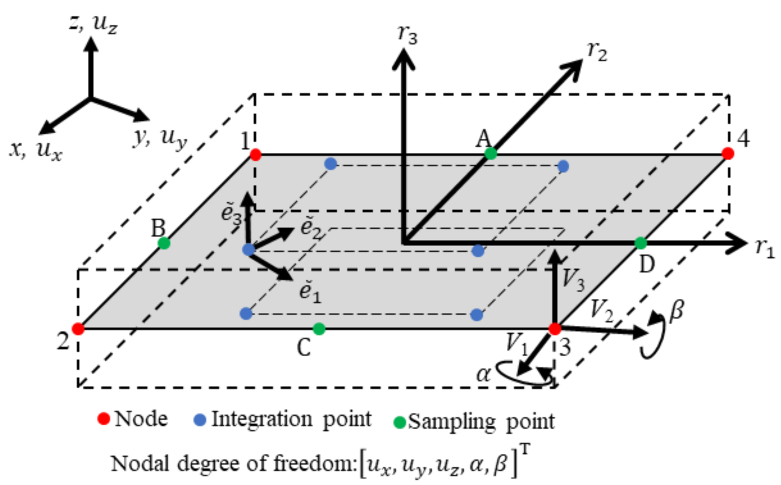

Fig. 3. Four-node MITC shell element.

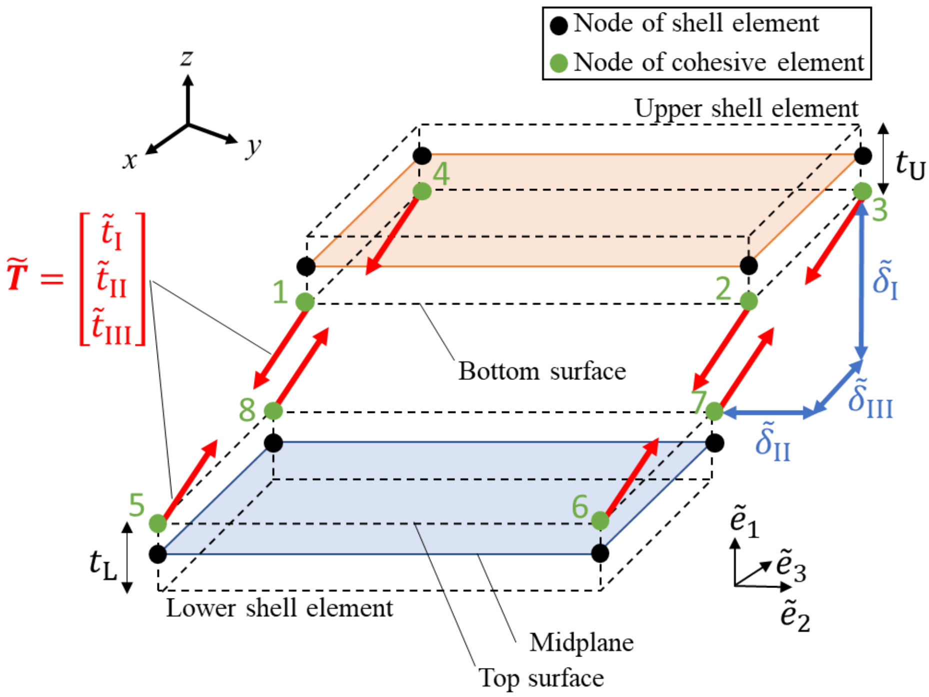

Fig. 4. Cohesive element between shell elements.

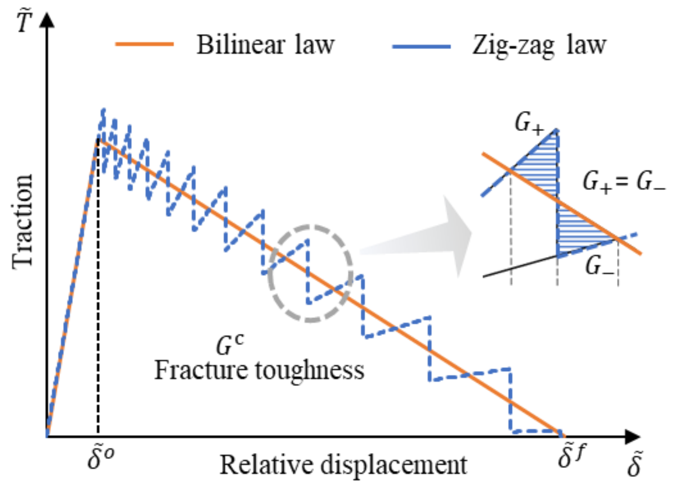

Fig. 5. Zig-zag traction–separation law of CZM.

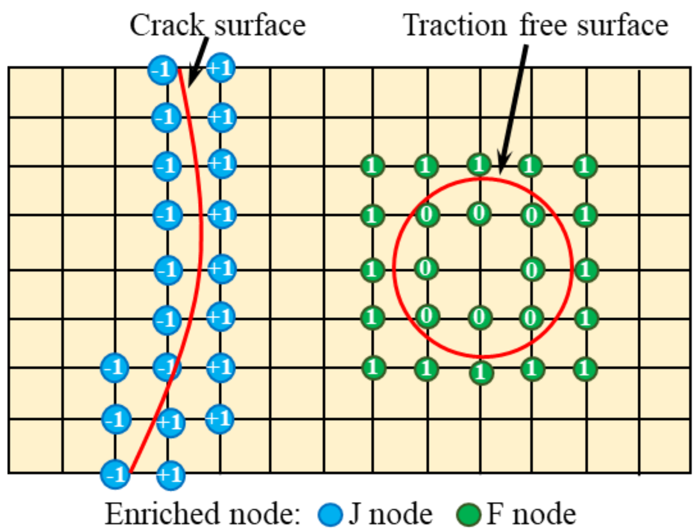

Fig. 6. Enriched nodes of a crack surface and free edge using the XFEM functions.

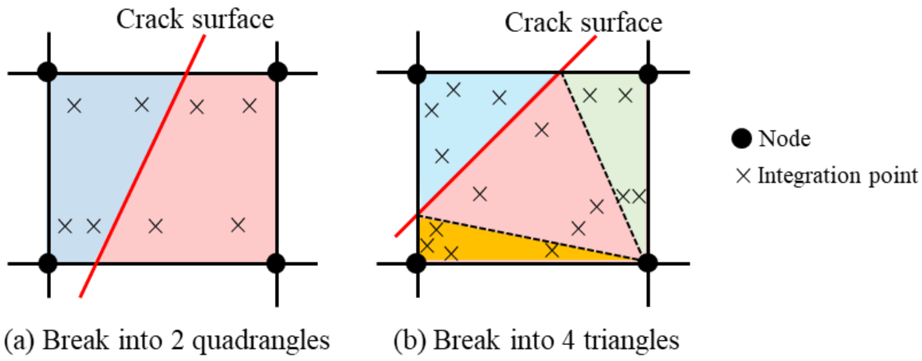

Fig. 7. Element division for Gaussian integration. (a) Break into 2 quadrangles and (b) 4 triangles.

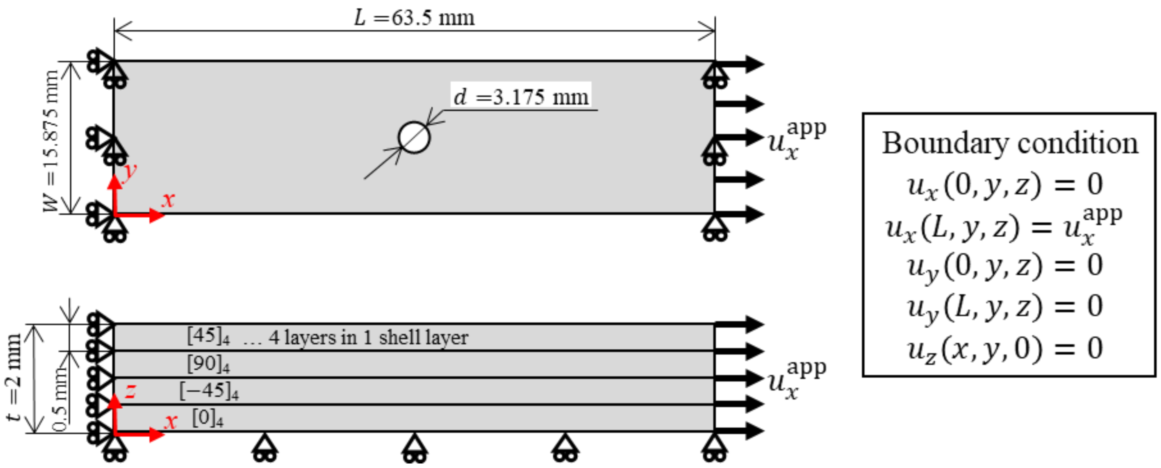

Fig. 8. Dimension and boundary condition of $[45_4/90_4/\text{-}45_4/0_4]_s$ laminate with a hole.

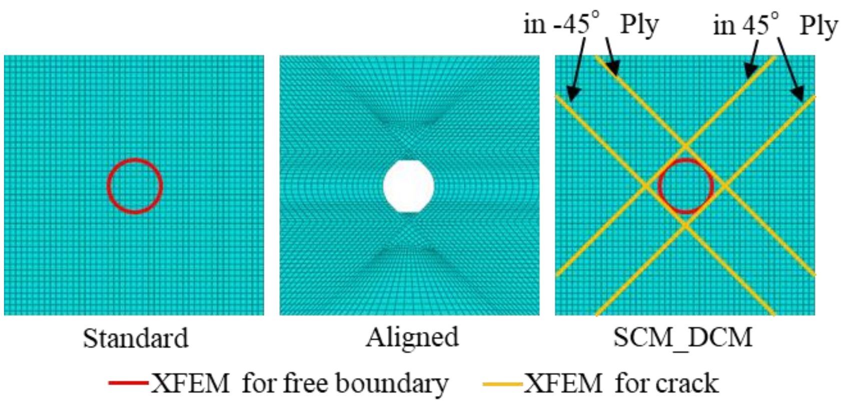

Fig. 9. Finite element mesh around the hole in the three models: (a) Standard, (b) Aligned, and (c) SCM_DCM.

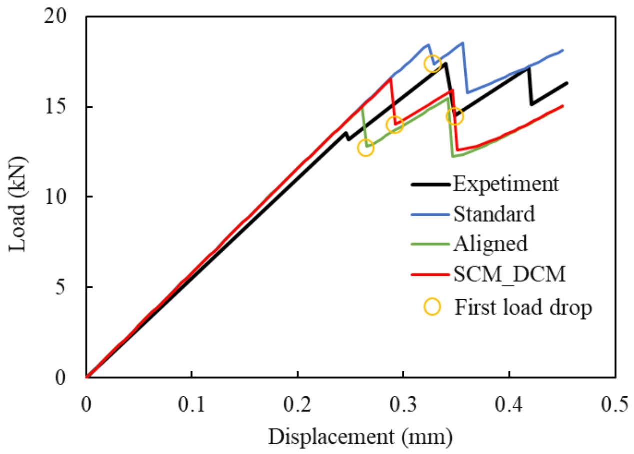

Fig. 10. Load–Displacement curves of the IM7/8552 $[45_4/90_4/\text{-}45_4/0_4]_s$ laminate obtained experimentally [22,51] and by using the three models.

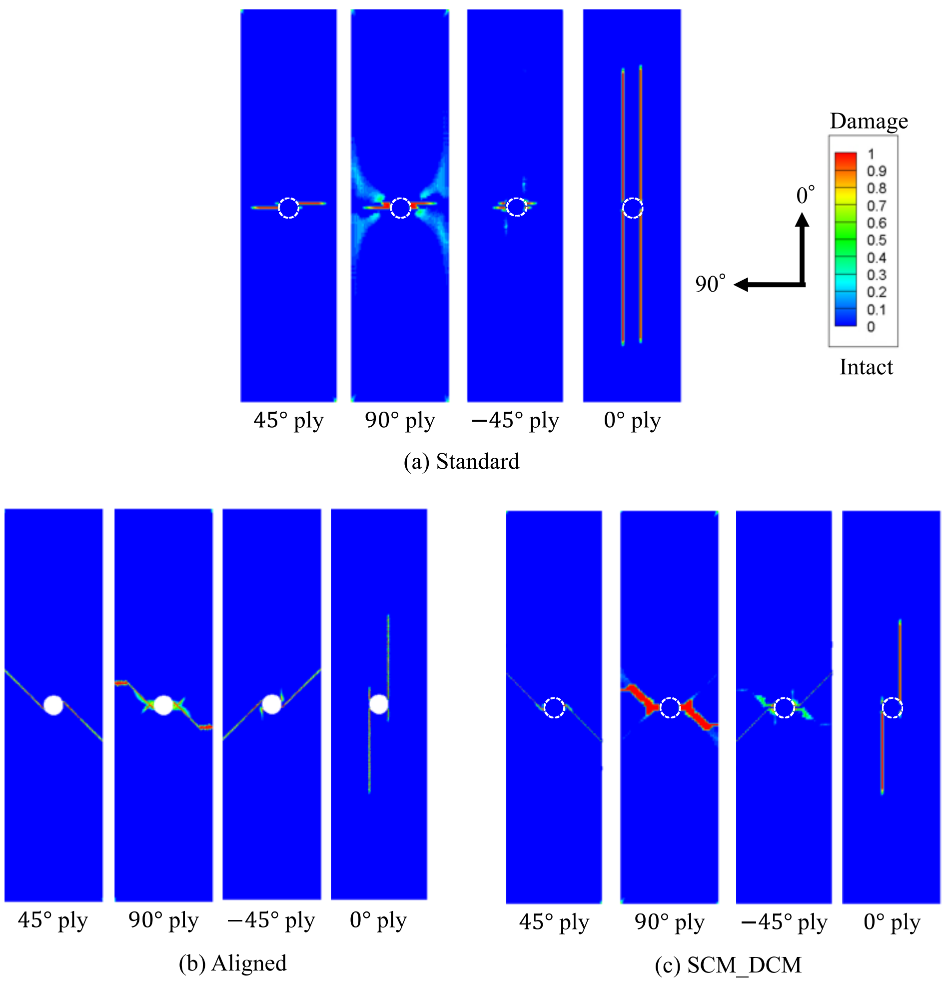

Fig. 11. Numerical results of matrix crack distributions of (a) Standard, (b) Aligned, and (d) SCM_DCM models after the first load drop. The dotted white line represents the circular hole modeled by XFEM.

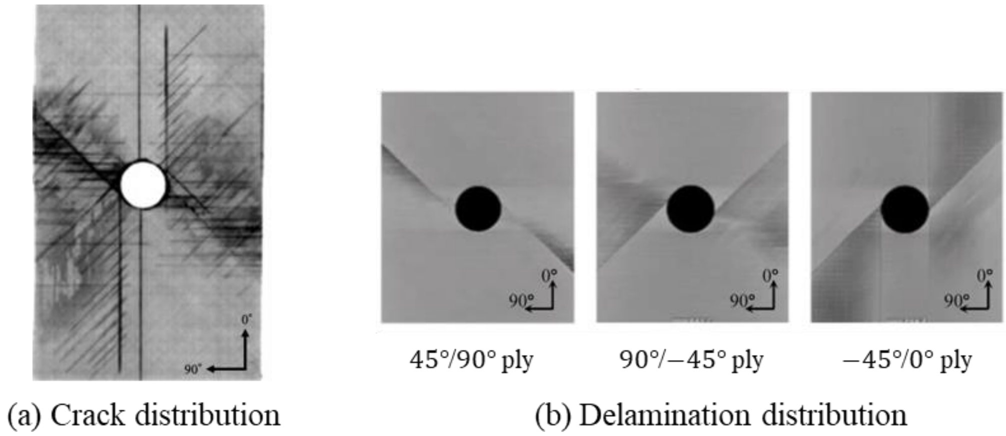

Fig. 12. X-lay images of (a) matrix crack [22] and (b) delamination [23] failure patterns of the IM7/8552 $[45_4/90_4/\text{-}45_4/0_4]_s$ laminate after the first load drop.

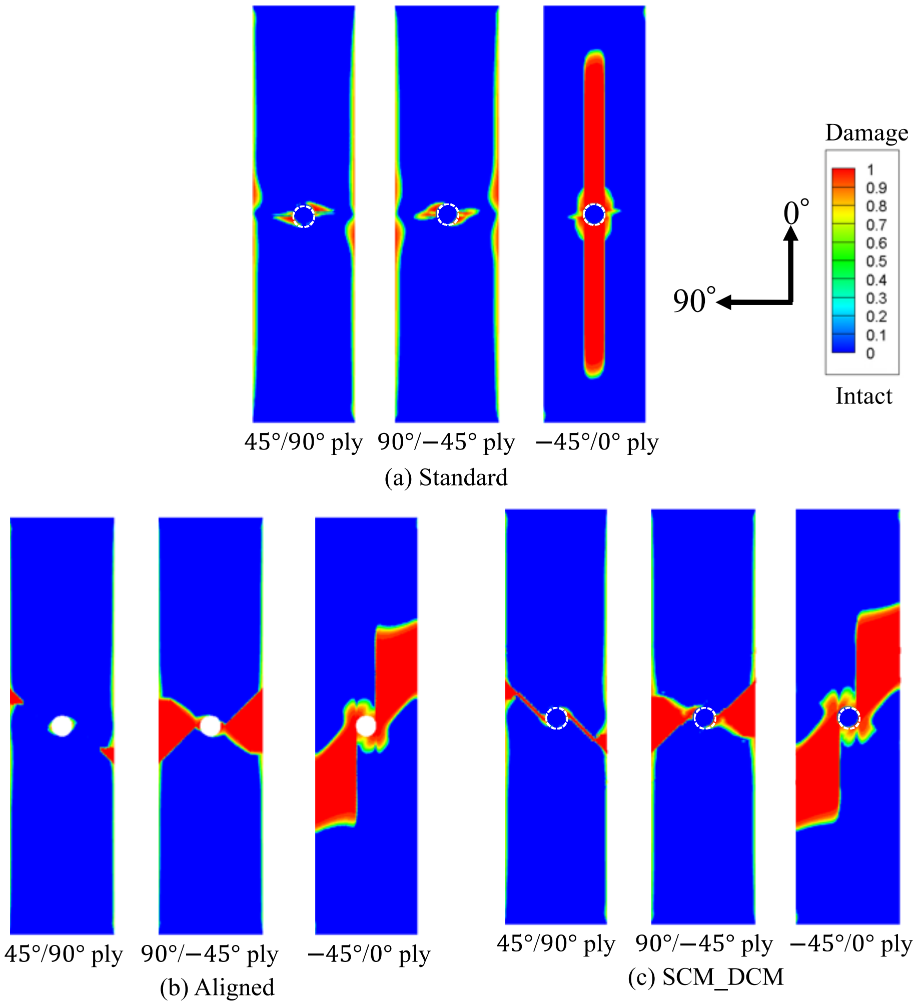

Fig. 13. Numerical results of delamination distributions of (a) Standard, (b) Aligned, and (c) SCM_DCM models after the first load drop. The dotted white line represents the circular hole modeled by XFEM.

x: with gap

Ply	Angle	Gap
1	45	
2	90	x
3	-45	
4	0	
5	45	
6	90	x
7	-45	
8	0	
9	0	
10	-45	
11	90	x
12	45	
13	0	
14	-45	
15	90	x
16	45	

(a) Stack sequence

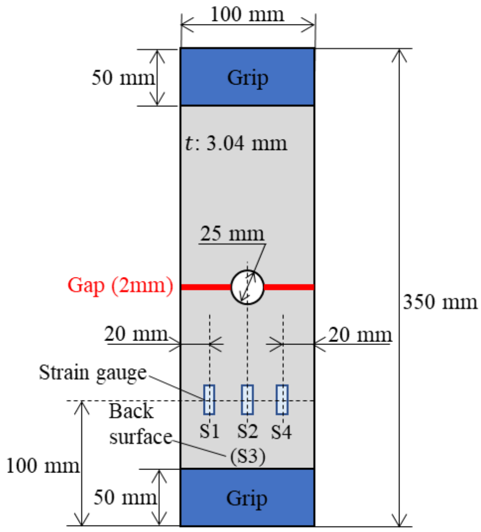

(b) Dimensions

Fig. 14. (a) Stacking sequence and (b) dimensions of the open hole tensile test specimen.

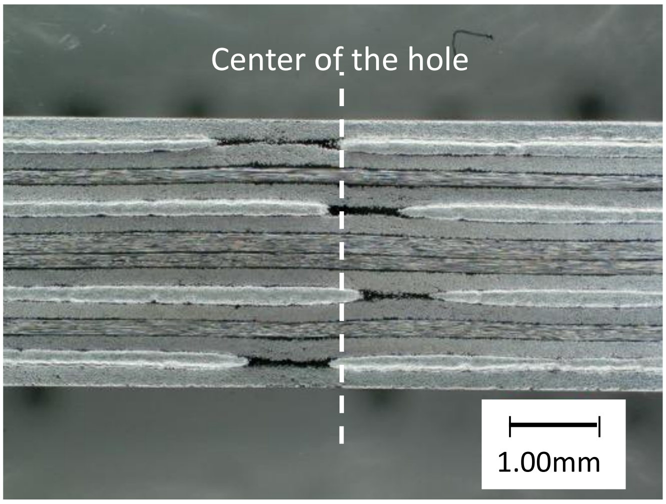

Fig. 15. Edge view of the specimen with gaps near the hole.

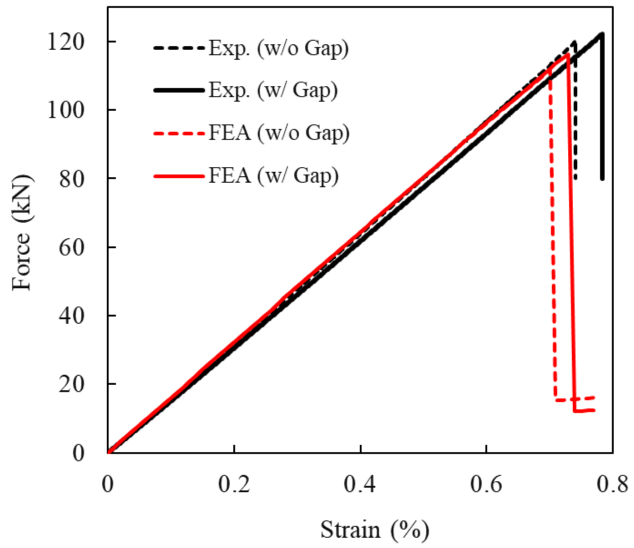

Fig. 16. Load–Strain curves of the T800S/3900-2B $[45/90/-45/0]_{2s}$ open hole laminate with and without gaps obtained experimentally and through FEA.

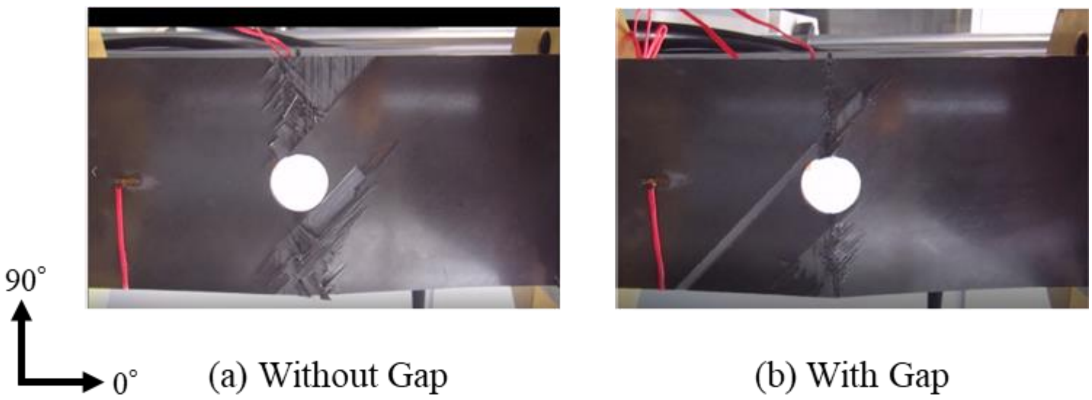

Fig. 17. Photographs of failure of specimen (a) without gaps and (b) with gaps in 90° plies.

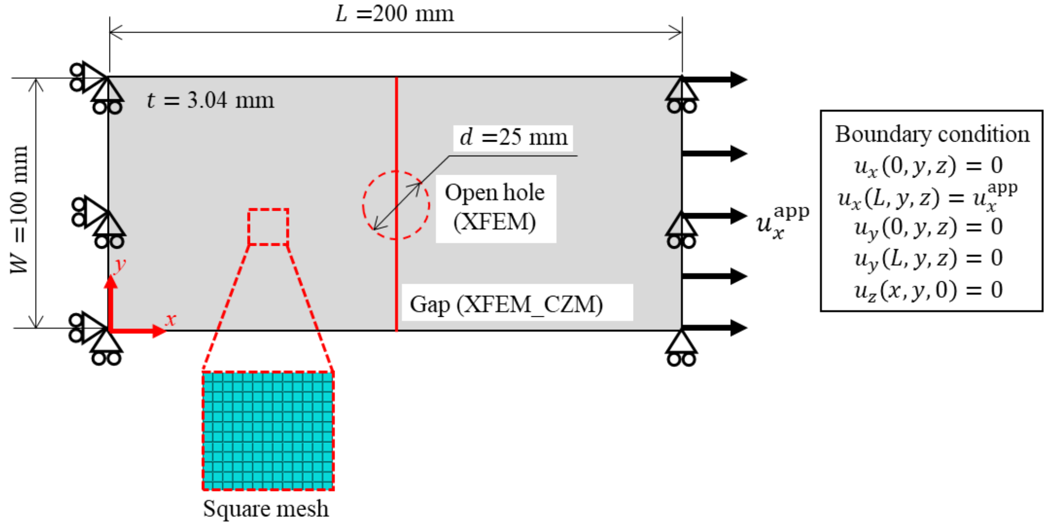

Fig. 18. Dimension and boundary condition of the $[45/90/\text{-}45/0]_{2s}$ open hole laminate with gaps in 90° plies.

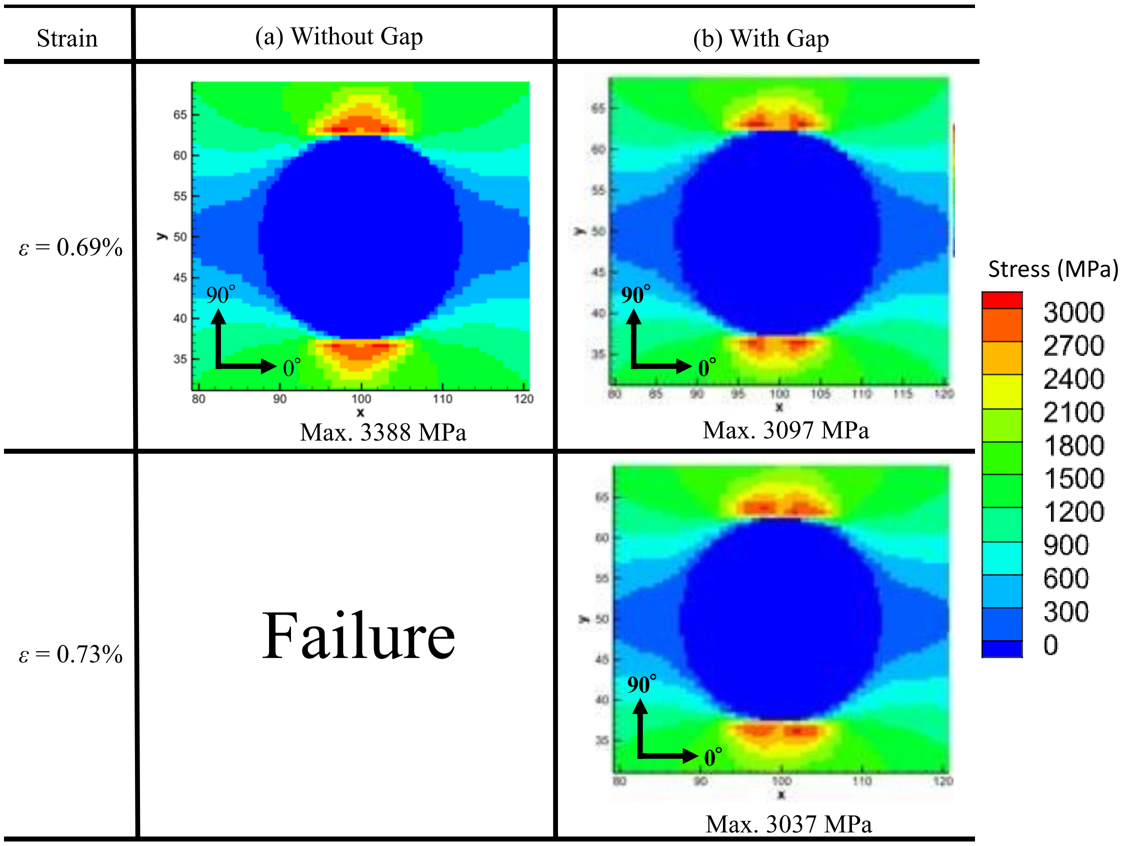

Fig. 19. Axial stress distribution of 0° ply (Ply 4) in the laminate (a) without and (b) with gaps in 90° plies immediately before final failure.

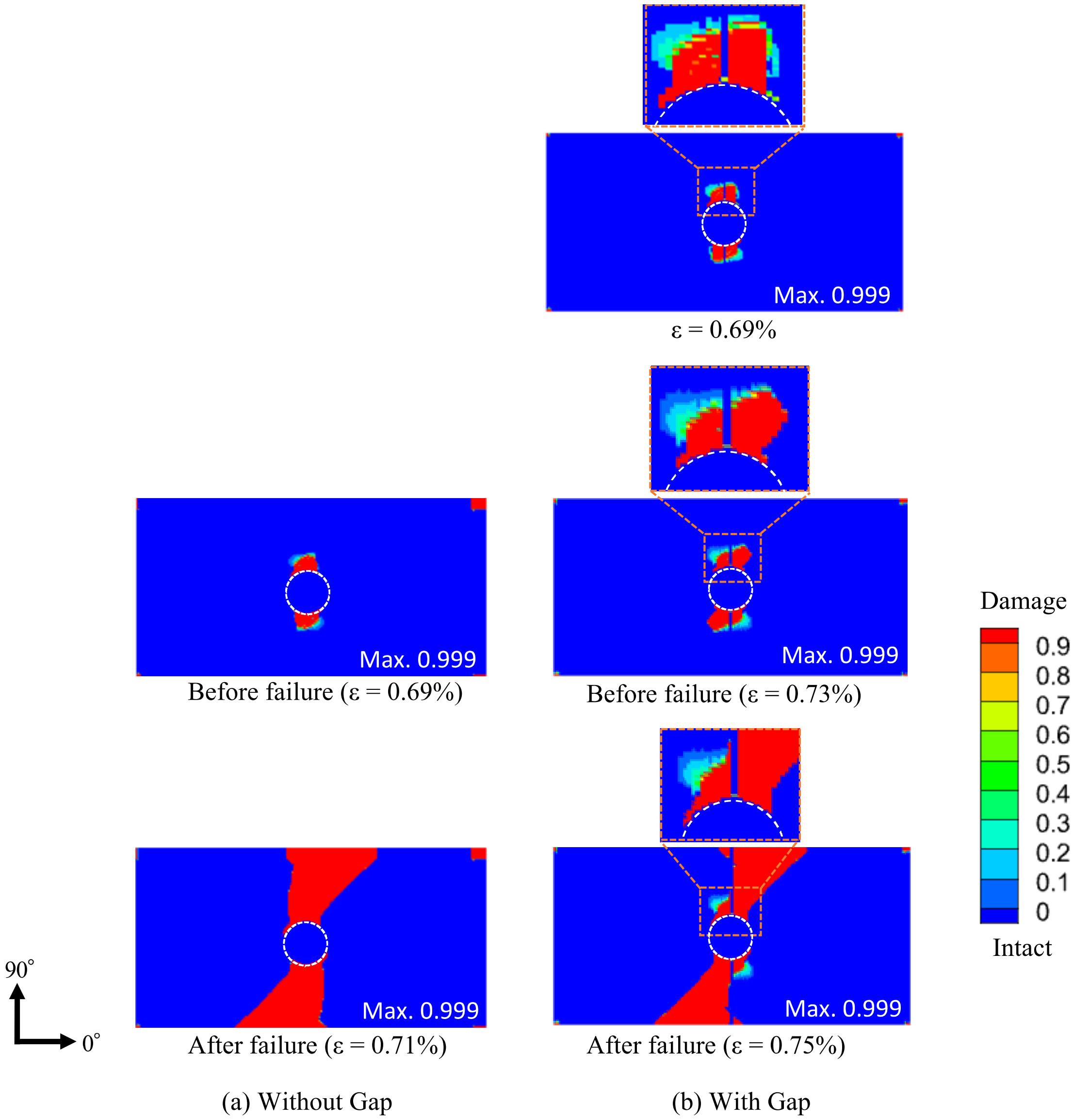

Fig. 20. Matrix crack distribution in 90° ply (Ply 2) immediately before and after final failure: (a) without and (b) with gaps in 90° plies. The dotted white line represents the circular hole modeled by XFEM.

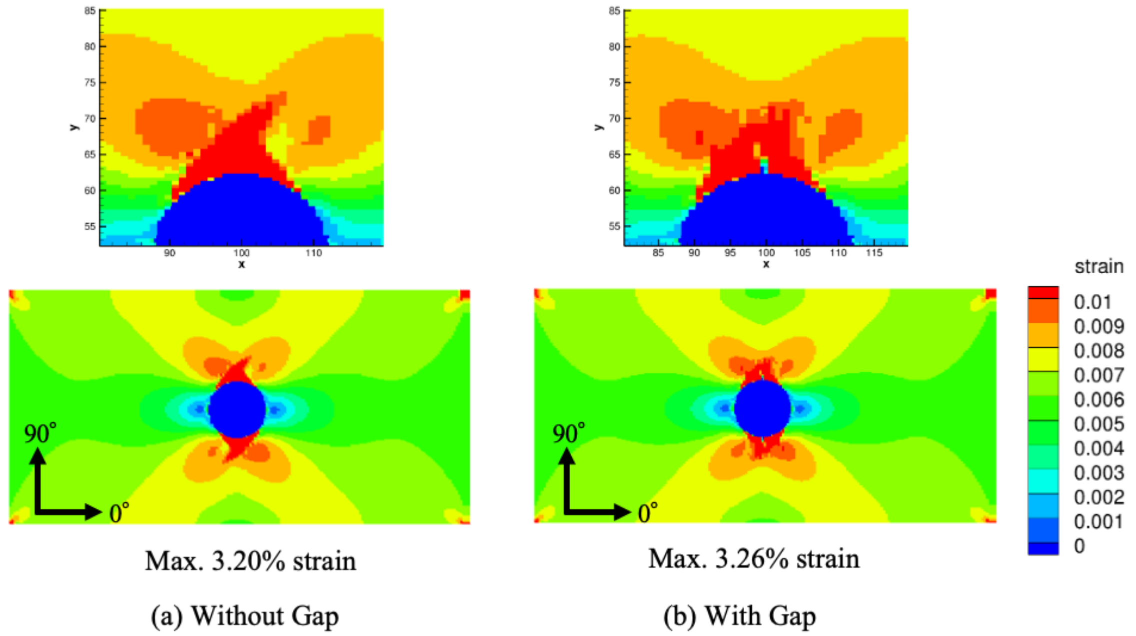

Fig. 21. Axial strain distribution of 90° ply (Ply 2) in the laminate (a) without or (b) with gaps in 90° plies at 0.69% applied strain.

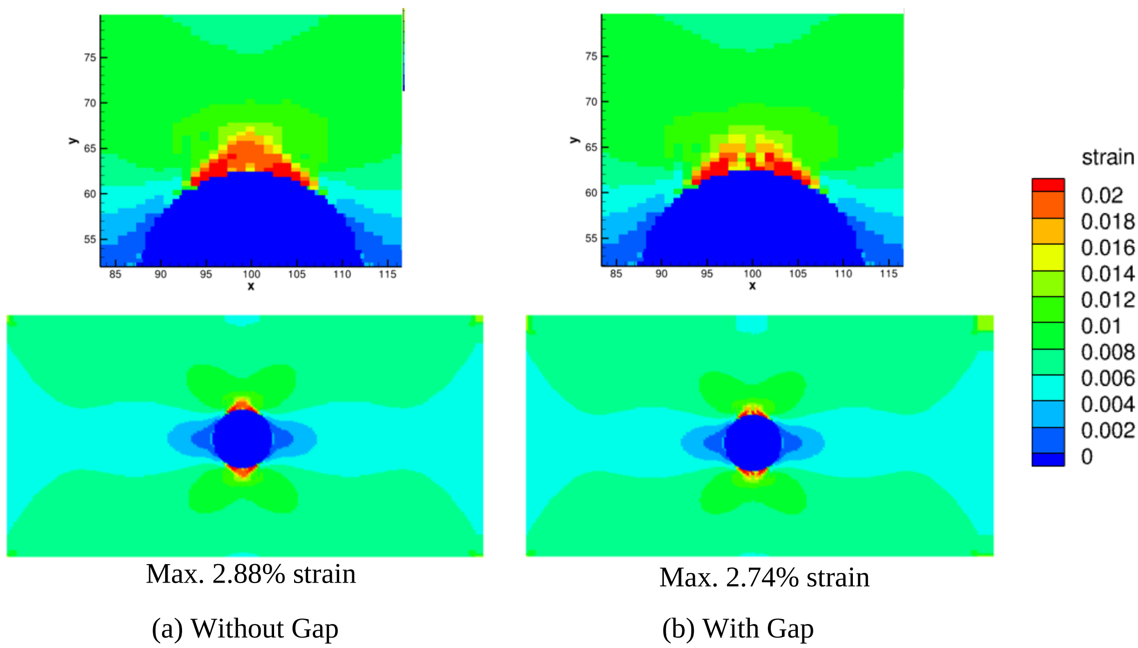

Fig. 22. Axial strain distribution of 90° ply (Ply 6) in the laminate (a) without or (b) with gaps in 90° plies at 0.69% applied strain.

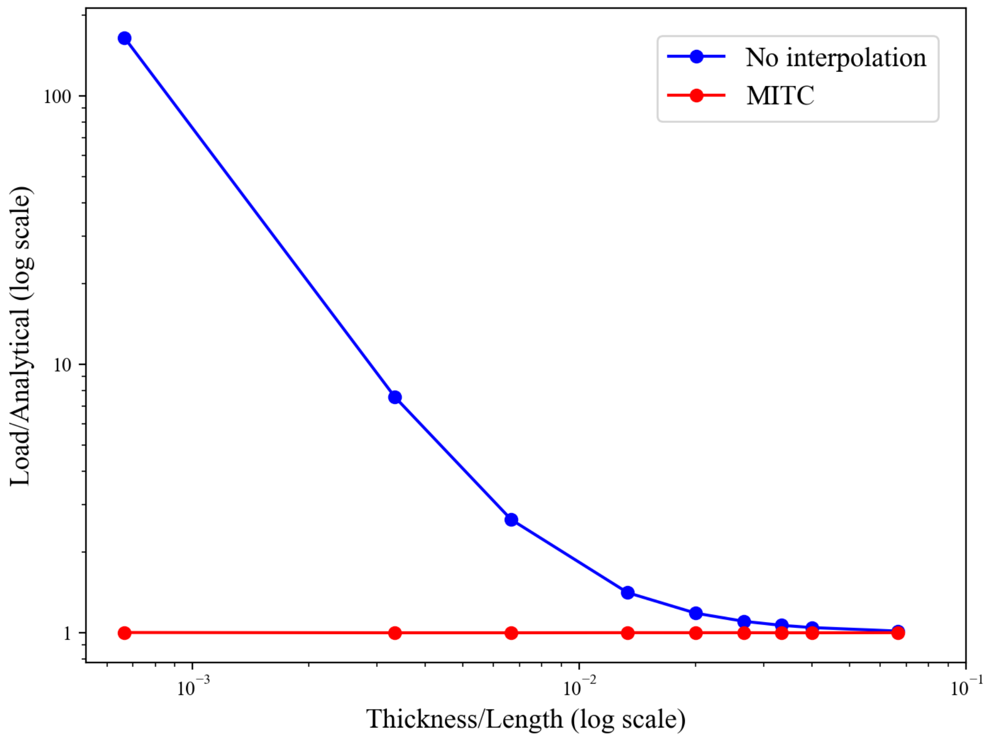

Fig. A.1. Comparison of loads for pure bending with varying thickness.

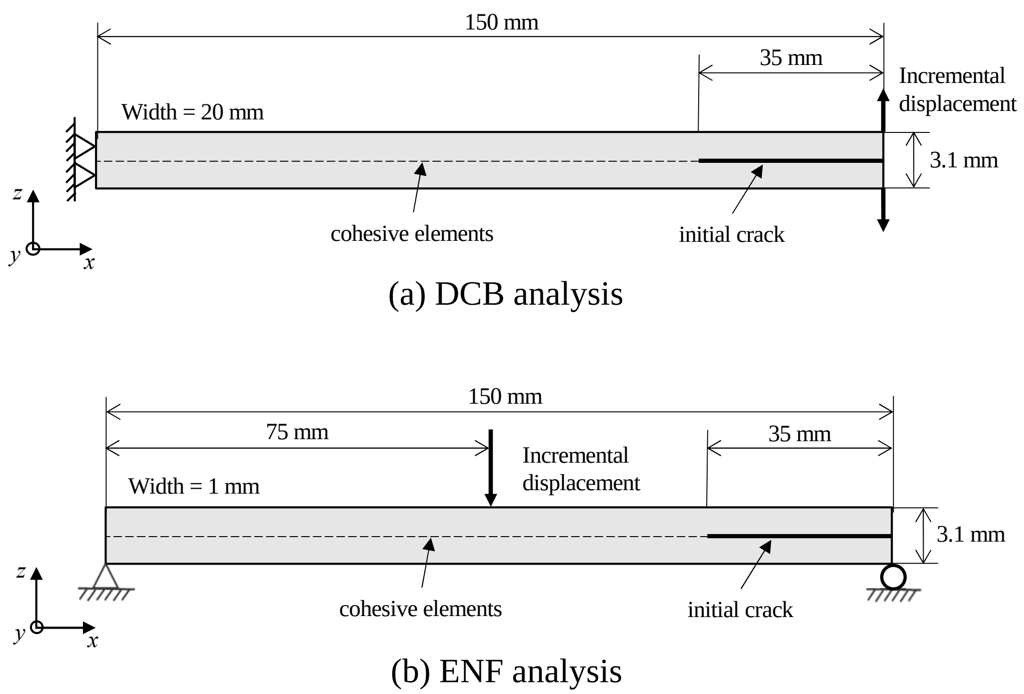

Fig. B.1. Simulation models and boundary conditions for (a) DCB and (b) ENF analyses using cohesive elements.

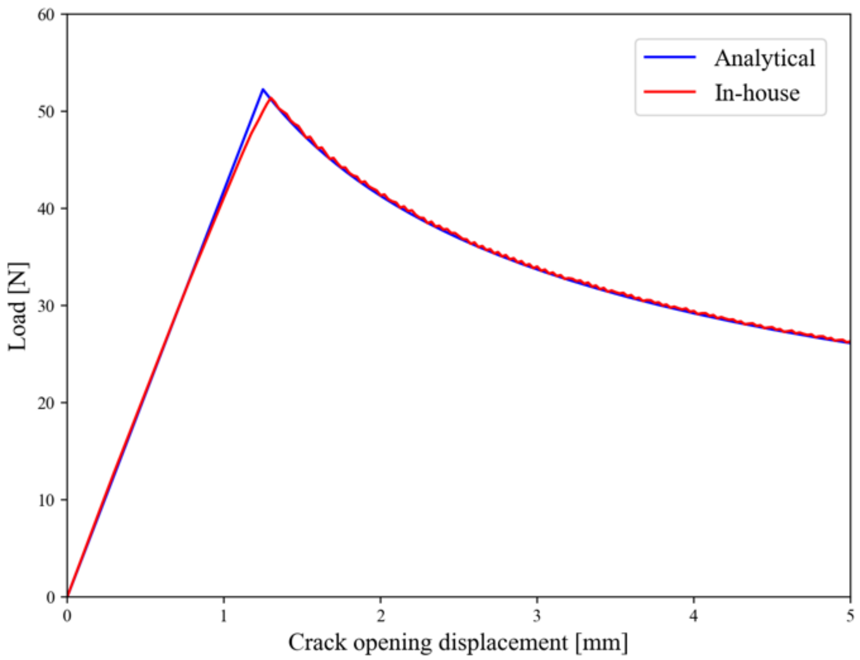

(a) DCB analysis

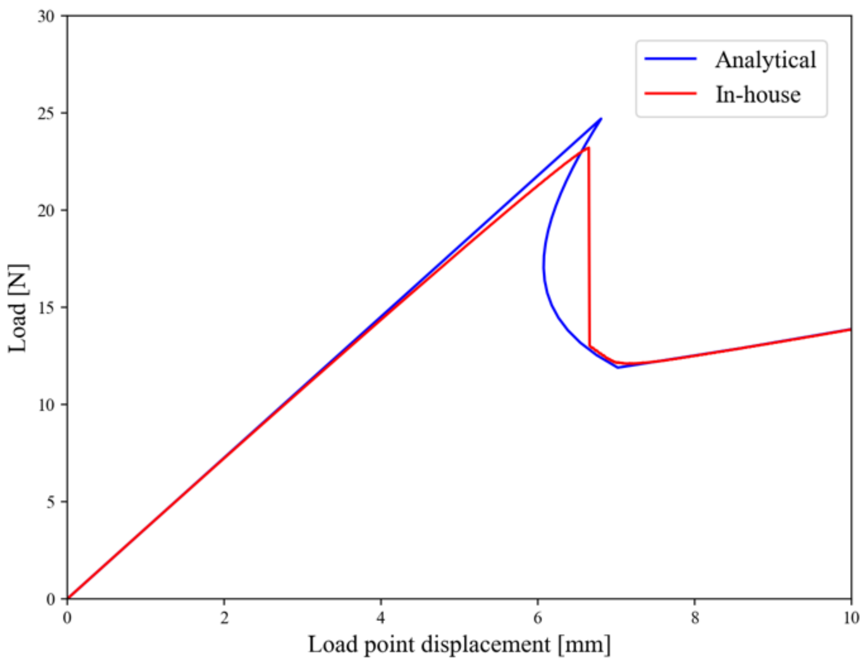

(b) ENF analysis

Fig. B.2. Comparisons of load-displacement curves for (a) DCB and (b) ENF analysis using cohesive elements.